Gravity and magnetic models at Rangitoto Volcano, Auckland Volcanic Field, New Zealand: Implications for basement control on magma ascent

Article *in* Journal of Volcanology and Geothermal Research · June 2023

DOI: 10.1016/j.jvolgeores.2023.107824

3 authors, including:

Alutsyah Luthfian
University of Auckland

Craig A. Miller
GNS Science

Journal of Volcanology and Geothermal Research 439 (2023) 107824

Contents lists available at ScienceDirect

Journal of Volcanology and Geothermal Research

journal homepage: www.journals.elsevier.com/journal-of-volcanology-and-geothermal-research

Gravity and magnetic models at Rangitoto Volcano, Auckland Volcanic Field, New Zealand: Implications for basement control on magma ascent

Alutsyah Luthfian [a,*], Jennifer D. Eccles [a], Craig A. Miller [b]

[a] School of Environment, The University of Auckland, Auckland, New Zealand
[b] GNS Science, Wairakei Research Centre, Taupō, New Zealand

ARTICLE INFO

Keywords:
Auckland Volcanic Field
Gravity and magnetic modeling
Monogenetic volcanism
Geophysics
Dyke intrusion

ABSTRACT

In small-volume volcanism, pre-existing crustal structures can influence magma ascent processes. Rangitoto volcano in the Auckland Volcanic Field, New Zealand, provides a possible example of magma-structure interaction as this volcano was emplaced adjacent to an outcrop of a regional-scale basement fault, the Islington Bay Fault. In this study, we evaluated the magmatic plumbing system of Rangitoto using gravity and magnetic data acquired over the volcano and the adjacent, non-volcanic Motutapu Island. We modelled the Rangitoto internal architecture and magma plumbing using 2.5D forward and 3D inverse modelling methods. Both models are constrained by petrophysical data, while drill hole logs are only used to constrain the 2.5D model. Our model endmembers suggest that parallel magma pathways are present below the Rangitoto summit cones. In 3D magnetic models, this is evidenced by a fault-aligned pair of high-susceptibility bodies. Interpreting our models in conjunction with previously published geological and geophysical models allows us to hypothesise that the fault-parallel alignment of Rangitoto magma pathways reflects the primary influence of the Islington Bay Fault over the Rangitoto magma ascent. Magma diversion at shallow levels by other finer structures intersecting and adjacent to the fault could explain why Rangitoto erupted 3.5 km west of the Islington Bay Fault surface trace.

1. Introduction

A volcanic eruption represents an endpoint of a magma ascent pathway that starts from the partial melting site in the mantle (Corvec et al., 2013; Brenna et al., 2011) or from the crustal magma reservoir (France et al., 2016; Yu et al., 2020). Along the pathway, magma intrudes as dykes whose trajectory can be influenced by crustal structures and regional or local stress fields (Rivalta et al., 2015; Martí et al., 2016). Pre-existing crustal structures can represent a zone of local weakness that a rising magma can utilise to travel upward (Gaffney et al., 2007). However, the utilisation of pre-existing structures may not always happen (e.g. in West Arabia; Duncan et al., 2016) if magma pressure is lower than the horizontal stresses acting on the structural plane (Delaney et al., 1986).

Lineaments of vents in volcanic fields are suggestive of local structural influence on magma ascent process (Corvec et al., 2013; Mazzarini, 2003; van den Hove et al., 2017). In the Michoacan-Guanajuato Volcanic Field (Mexico), a string of volcanoes appears along an ENE-striking fault system (Gómez-Vasconcelos et al., 2020). The alignment of volcanoes in the Lassen Volcanic Region (USA) parallels the NNW-trending normal faults (Guffanti et al., 1990). The Chaine des Puys (France) volcanoes are aligned parallel to the N-S trending Limagne basement fault (Boivin and Thouret, 2013).

The Auckland Volcanic Field (AVF) in New Zealand (NZ) is among those volcanic fields where vent lineaments have been recognised (Bebbington, 2015; Corvec et al., 2013), and some of them are correlated with mapped structures (e.g. Wiri Mountain; Foote et al., 2022). Some other AVF vents (e.g., Maungataketake, Waitomokia, and Mangere) are aligned along an NNE to NE-trending line (Bebbington, 2015) parallel to Miocene structures mapped around the volcanic field (Edbrooke, 2001). Rangitoto, the youngest and most voluminous AVF volcano, exhibits two N-S-aligned vents next to a surface expression of the NNW-SSE-trending Islington Bay Fault (Kenny et al., 2012) and proposed extensions of the Karaka and Bucklands Beach faults (Fig. 1). Seismic tomography by Ensing et al. (2022, modelling the 0.5 km downward) suggests that a deep crustal shear wave velocity discontinuity exists under Rangitoto to ~ 10 km depth, which can be associated with the Islington Bay Fault (Kenny et al., 2012) or older structures derived from Mesozoic deformations of the Waipapa Terrane (Eccles et al., 2005). From the Rangitoto vent alignment, combined with its

* Corresponding author.
E-mail address: alut525@aucklanduni.ac.nz (A. Luthfian).

https://doi.org/10.1016/j.jvolgeores.2023.107824
Received 8 February 2023; Received in revised form 7 May 2023; Accepted 14 May 2023
Available online 12 June 2023

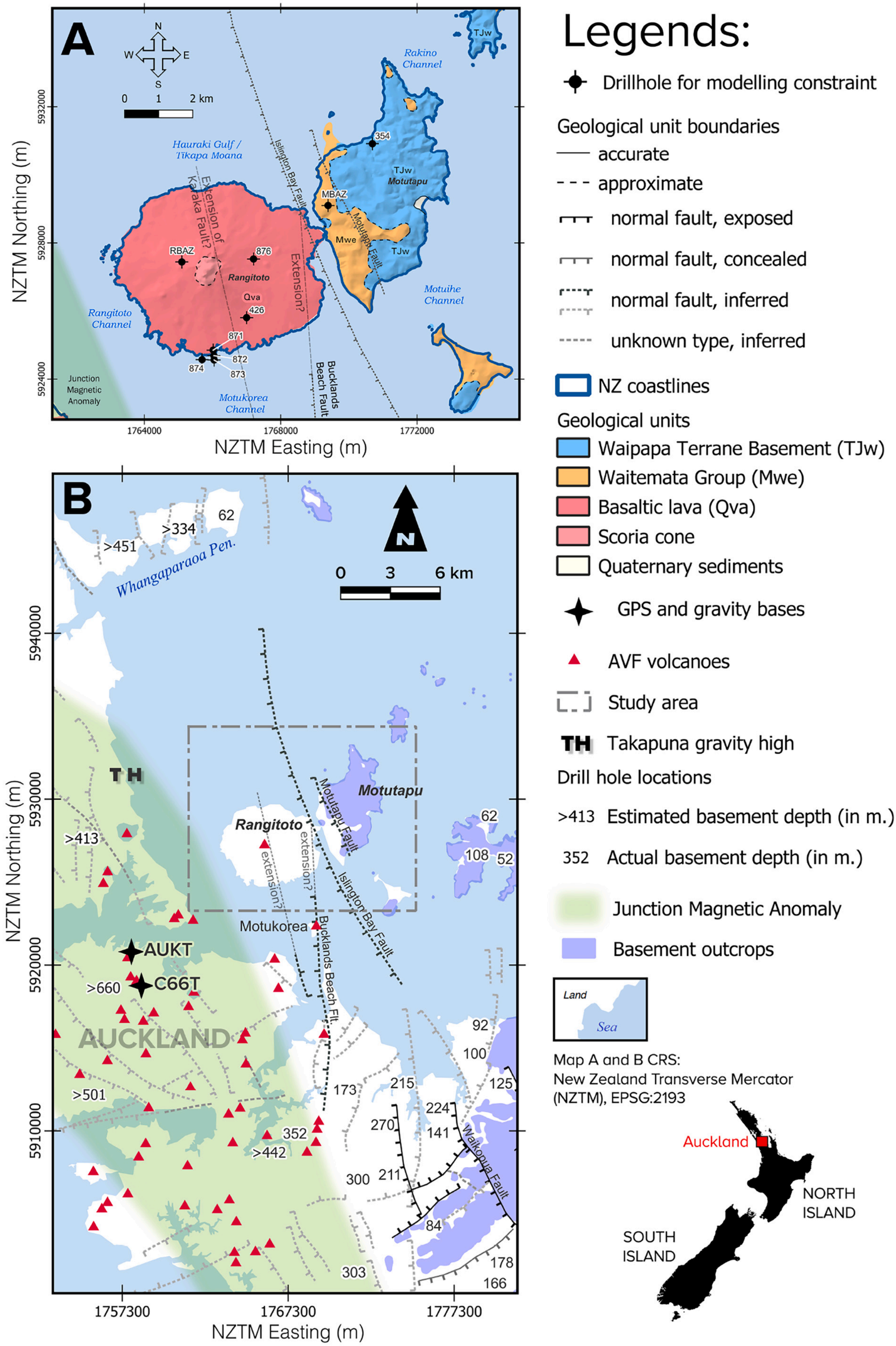

(caption on next page)

Fig. 1. (A) Geological map of Rangitoto and Motutapu Islands. (B) Structural geology map of the Auckland Isthmus and its surroundings. The extent of map A is marked with a grey dashed line. Ticks on fault line symbols mark the downthrown side. Relevant faults for this study are named and thickened on the figures. Geological units are according to NZL GNS 1:250 K Geology (GNS Science, 2020); volcano locations are from Leonard et al. (2017); fault lines are synthesised from NZL GNS 1:250 K Geology (GNS Science, 2020), Kenny et al. (2012), Kenny (2013b), Kenny (2013a); drill hole logs data are from Linnell et al. (2016), PETLAB (Strong et al., 2016), and New Zealand Geotechnical Database (NZGD; EQC, 2012); extent of the Junction Magnetic Anomaly (JMA) is interpreted from published magnetic anomaly map by Eccles et al. (2005) and Hunt and Syms (1977). Basemap and shoreline data is from ESRI and Land Information New Zealand (LINZ).

close proximity to surface faults and crustal shear wave velocity discontinuity, we hypothesise that there is a possibility of crustal structure-dyke ascent interplay prior to the eruption and the formation of Rangitoto.

In this study, we investigate Rangitoto's volcanic and sub-volcanic plumbing system using 2.5D forward and 3D inverse modelling of new gravity and existing airborne magnetic data. Previous works have demonstrated that simultaneous interpretation of 2.5D and 3D gravity and magnetic models could assist in determining internal volcanic architecture, e.g. Paoletti et al. (2009), Cocchi et al. (2017), Blaikie et al. (2014). Creation of these new models is constrained by the available geological, petrological, and drill hole log data. The models also allow us to investigate relationships between crustal structure and the location of Rangitoto vents. Insights gained from this study may be applicable to the remainder of the AVF or other volcanic fields in the world where structural control to magma ascent can only be inferred, e.g., the Newer Volcanic Province in South Australia (Holt et al., 2013), Pali Aike volcanic field, Argentina (Ross et al., 2011), and Al Haruj Volcanic Field, Libya (Elshaafi and Gudmundsson, 2016).

1.1. Rangitoto volcanism

The Auckland Volcanic Field (AVF) consists of 53 known small-volume volcanoes that are uniformly basaltic in composition (Hopkins et al., 2020; Hopkins et al., 2017, Fig. 1B). Huang et al. (1997) and Brenna et al. (2018) interpret AVF vents to be fed by magma batches ascending rapidly from a partial melting site estimated at 80 to 140 km deep in the mantle. To date, the AVF has erupted a total of 1.7 km^3 of dense-rock equivalent (DRE) magma, creating tuff rings, maars, lava fields, and scoria cones (Kereszturi et al., 2013). Among AVF volcanoes, Rangitoto is the youngest, erupted at ca. 1450 and 1500 AD (Needham et al., 2011, Fig. 1), and the most voluminous (~ 0.7 km^3 DRE volume; Kereszturi et al., 2013). It erupted 3.5 km west of a topographic scarp of a mapped NNW-SSE trending basement fault (Islington Bay Fault; Kenny et al., 2012, Fig. 1).

Rangitoto (260 m above sea level) is an approximately circular volcanic shield island with diameter of ~ 5 to 6 km (Fig. 1). Lava fields occupy 99.98% of the total Rangitoto surface area and dip seaward at 4 to 12 degrees (Needham et al., 2011). At the centre of Rangitoto is overlapping scoria cones made of scoria and tephra successions (Kereszturi and Németh, 2016, Fig. 1). The North and South Cone are defined based on differences in observed morphology and geochemistry within the scoria cone complex (Needham et al., 2011). The North Cone is $\sim$ 300 m north of the South Cone, and their alignment is subparallel to the Islington Bay fault (Fig. 1A).

Drill hole logs and foraminiferal evidence suggest that the first eruption of Rangitoto occurred in a shallow marine setting (Linnell et al., 2016; Hayward et al., 2022). As the magma supply increased, later phases of the Rangitoto eruption built the subaerial scoria cones and a broad lava field (Smith and Németh, 2017). Radiocarbon dating of Rangitoto tephras preserved in lakes and swamps on the Motutapu Island suggest that the alkalic North Cone was formed ~ 1450 AD (Needham et al., 2011). The North Cone was then modified by the subsequent eruptions into a series of mounds and ridges which were then partially buried by the sub-alkalic South Cone (~ 1500 AD) and the lava field (Needham et al., 2011; Linnell et al., 2016). The South Cone has smooth flanks and a well-defined 60 m deep, 150 m wide summit crater (Needham et al., 2011). The lava field, giving Rangitoto its distinctive circular shield shape, extends and thins radially ~ 2 to 3 km from the base of central cones (e.g. ~ 128 m thick at "RBAZ" vs. ~ 17.4 m thick at "871", Fig. 1; Linnell et al., 2016; Strong et al., 2016). Different scenarios (e.g., Needham et al., 2011; Linnell et al., 2016; Hayward, 2017) for the growth of the Rangitoto have been postulated based on surface outcrops and core logs. Building from these, in this study we present a geophysically-informed model of the Rangitoto magma plumbing and its possible association to the crustal structures.

As Rangitoto is a conservation area and a highly important Maori cultural site (Hall, 2013), the non-invasive geophysical exploration techniques of gravity and magnetic surveys are utilised. Gravity and magnetic surveys exploit the strong density and magnetic susceptibility contrasts among, or between, volcanic and non-volcanic materials (Hinze et al., 2013). At the AVF, gravity and magnetic surveys have been used to interpret the subsurface geology, providing insights into the eruption dynamics and volcanic plumbing systems (e.g., Cassidy et al., 2007; Nunns and Hochstein, 2019; Affleck et al., 2001). Use of gravity and magnetic surveys on other small-volume volcanic fields worldwide is well established, e.g., Barde-Cabusson et al. (2013), Espindola et al. (2016), Hastings et al. (2021), Blaikie et al. (2014) and Aboud et al. (2015), where they interpret vent-structure relationship, internal volcanic architecture, presence of crustal magma intrusions, and the thickness of volcanic deposits.

1.2. Subvolcanic geology and faults

Drilling on the western ("RBAZ", Fig. 1A) and southern flanks of the volcano ("871", Fig. 1A) found that Rangitoto volcanic deposits overlie unconsolidated Quaternary marine sediments (Linnell et al., 2016; Strong et al., 2016) and highly weathered Waitemata Group (Linnell et al., 2016). Waitemata Group outcrops at the western side of Motutapu Island and consists of Miocene interbedded mudstone and sandstones (Edbrooke, 2001; Hayward and Brook, 1984). The Islington Bay Fault displaces both Waitemata Group and the underlying Waipapa Terrane metasedimentary basement, both of which are exposed on Motutapu Island (Edbrooke, 2001; Mayer, 1969, Fig. 1A).

To the west of Rangitoto, the Junction Magnetic anomaly (JMA, Fig. 1) geophysically marks what is interpreted as the buried basement transition of the Waipapa Terrane into the ultramafic Dun Mountain-Maitai terrane (Eccles et al., 2005; Williams et al., 2006). East of Rangitoto, lie the NNW-striking Islington Bay and Motutapu faults (Fig. 1; Kenny et al., 2012; Mayer, 1968). Spörli et al. (1989) interprets NNW-striking faults in Auckland as Cretaceous rift-related structures reactivated by the Miocene extension and uplift (Spörli and Rowland, 2007; Spörli et al., 1989). Being a product of extensional tectonic processes, it is likely that Islington Bay and Motutapu faults are normal faults, like other NNW-SSE striking faults in Auckland (Edbrooke, 2001), placing Rangitoto on the hanging wall of the fault plane. Evidence from seismic reflection sections suggests that Islington Bay and Motutapu faults continue under the sea north of Rangitoto and Motutapu islands (B. Davy, GNS, 2011, personal observation with Kenny et al., 2011). Additionally, the N-S trending Bucklands Beach and Karaka Fault extend from mainland Auckland towards the south of Rangitoto (Fig. 1; Kenny et al., 2012). Although their offshore extents are unknown, an extrapolation of Buckland Beach Fault could intersect Islington Bay Fault at northeastern Rangitoto shore, and an extension of Karaka Fault could pass beneath Rangitoto Island (Fig. 1A).

2. Data

2.1. Gravity data

We collected 79 new gravity measurements with LaCoste and Romberg G1094 relative gravimeter on Rangitoto and Motutapu Islands along accessible walking tracks. Ecological restrictions prevented data collection on the trackless northern flanks of Rangitoto. Gravity data are drift corrected using a local base station and tied to the NZ reference gravity station at point C66T on the mainland (Fig. 1B; Stagpoole et al., 2021), using GSolve (McCubbine et al., 2018). Precise positional data was acquired using the Trimble RTK R10 Global Positioning System (GPS) receiver and differentially post-processed to an accuracy of < 0.04 m in horizontal uncertainty and < 0.05 m in vertical uncertainty using the AUKT Global Navigation Satellite System (GNSS) station operated by GeoNet/GNS Science (GNS Science, 2022a), ~ 8 to 16 km from the survey area (Fig. 1B). The instrumental gravity data were converted to mGal, corrected for instrumental drift and tidal effect, and tied to the absolute reference station value to allow integration with pre-existing data (New Zealand land gravity database; GNS Science, 2012). Our higher-precision measurements superseded older gravity measurements by Milligan (1977).

The absolute gravitational acceleration values are computed to complete Bouguer anomaly (CBA) using procedures described in Hinze et al. (2013). The vertical reference elevation used is the GRS80 ellipsoid with ITRF96 reference frame. Because we use the ellipsoid as vertical datum, our CBA is technically a “gravity disturbance” (Hinze et al., 2005), however we choose to call it “anomaly” in this article for familiarity purposes.

Our CBA is calculated using a reduction density of $2.39\ \mathrm{g/cm^3}$ (Fig. 2), determined by the methods of Nettleton (1939), which search for a density that minimises the correlation of the Bouguer anomaly with topography. The reduction density is calculated using west-east Rangitoto-Motutapu profile data (Fig. 2), which passes four different geological units with different densities (basalt, scoria, Waitemata Group, and Waipapa metasediments; Fig. 1A). Hence, the reduction density represents a composite of these rock types. Using only the Rangitoto portion of the west-east profile, we calculate the density of surface volcanic material (vesicular basalt and scoria) to be $2.22\ \mathrm{g/cm^3}$. Meanwhile, the Motutapu portion of the west-east profile yields $2.49\ \mathrm{g/cm^3}$ as the calculated density of near-surface lithology (Waipapa metasediment covered by $\leqslant \sim 90$ m of Waitemata Group). Therefore, the use of $2.39\ \mathrm{g/cm^3}$ over the entire profile underestimates the resultant gravity over Rangitoto and overestimates that over Motutapu.

We calculated terrain corrections using Geosoft Oasis Montaj implementation of Kane (1962) and Nagy (1966) algorithms. The gravitational effect of the terrain was computed for four different correction radii (0.4, 5, 22, and 167 km). LIDAR data, with one-metre horizontal resolution and 0.2 m vertical uncertainty (LINZ, 2016a), was used for the 0.4 km correction radius. Other radii used combined DEM-bathymetric files with resolutions ranging from 5 m (0.5 m assumed vertical uncertainty) to 250 m (1 m assumed vertical uncertainty; LINZ, 2016b; Mackay et al., 2012).

The uncertainty of the final Bouguer gravity anomaly (Fig. 3A) is $\leqslant$ 0.10 mGal, except at point D2-15, where it is 0.51 mGal due to poor GPS reception in dense vegetation (see Fig. 3A and C for location, Supplementary Material 1). Omitting point D2-15, the terrain correction is the largest contributor of data uncertainty (Supplementary Material 1). Terrain correction uncertainty is calculated as the difference between terrain correction values produced by the DEM plus and minus their elevation uncertainties. Finally, data from the New Zealand Land gravity database were given an uncertainty value of 0.5 mGal since their positioning was done in the pre-GPS era but with comparable gravimeters (GNS Science, 2012).

The complete Bouguer anomaly (CBA) map of Rangitoto and Motutapu (Fig. 3A) shows a gravity low on the eastern part of Rangitoto bordered by two highs, one to the east on Motutapu and the other on the western shore of Rangitoto. This gravity low is spatially correlated with the basaltic lava field and appears west of the Islington Bay fault which correlates to a steep gradient (cf. Figs. 3A and 1A). On the other hand, the Motutapu Fault is not distinguishable in the gravity anomaly maps (Fig. 3). The steep eastern boundary of Rangitoto low stands in contrast to its western boundary, spatially correlated to a proposed extension of Karaka fault, where CBA rises gradually toward the west (Fig. 3A). Within this gravity low is a small elongate gravity high observed at the location of Rangitoto scoria cones (cf. Figs. 3A and 1A). The gravity high over Motutapu Island corresponds to shallow basement or basement outcrops (Fig. 1A).

2.2. Magnetic data

We compiled a magnetic anomaly dataset from two aeromagnetic surveys acquired in July 2000 and January 2001 (Supplementary Material 2; Eccles, 2003). The aeromagnetic surveys were flown at a nominal altitude of ~ 430 m above sea level with a general bearing of 60° E (Fig. 4B), perpendicular to the trend of JMA (Eccles et al., 2005;

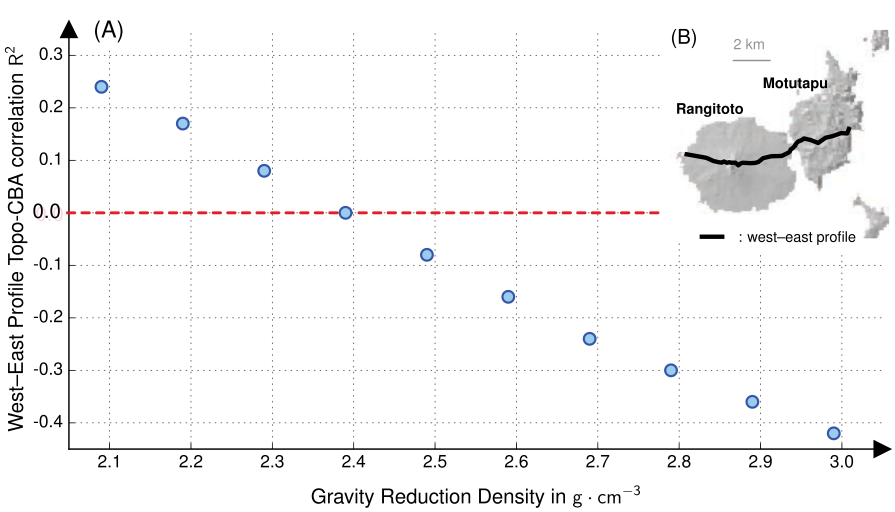

Fig. 2. (A) Pearson correlation R^2 between topographic variation and complete Bouguer anomaly along west-east profile on Rangitoto and Motutapu Islands (see inset B) as a function of reduction density. A density of $2.39\ \mathrm{g/cm^3}$ minimised the correlation of Bouguer anomaly with topography across the entire profile.

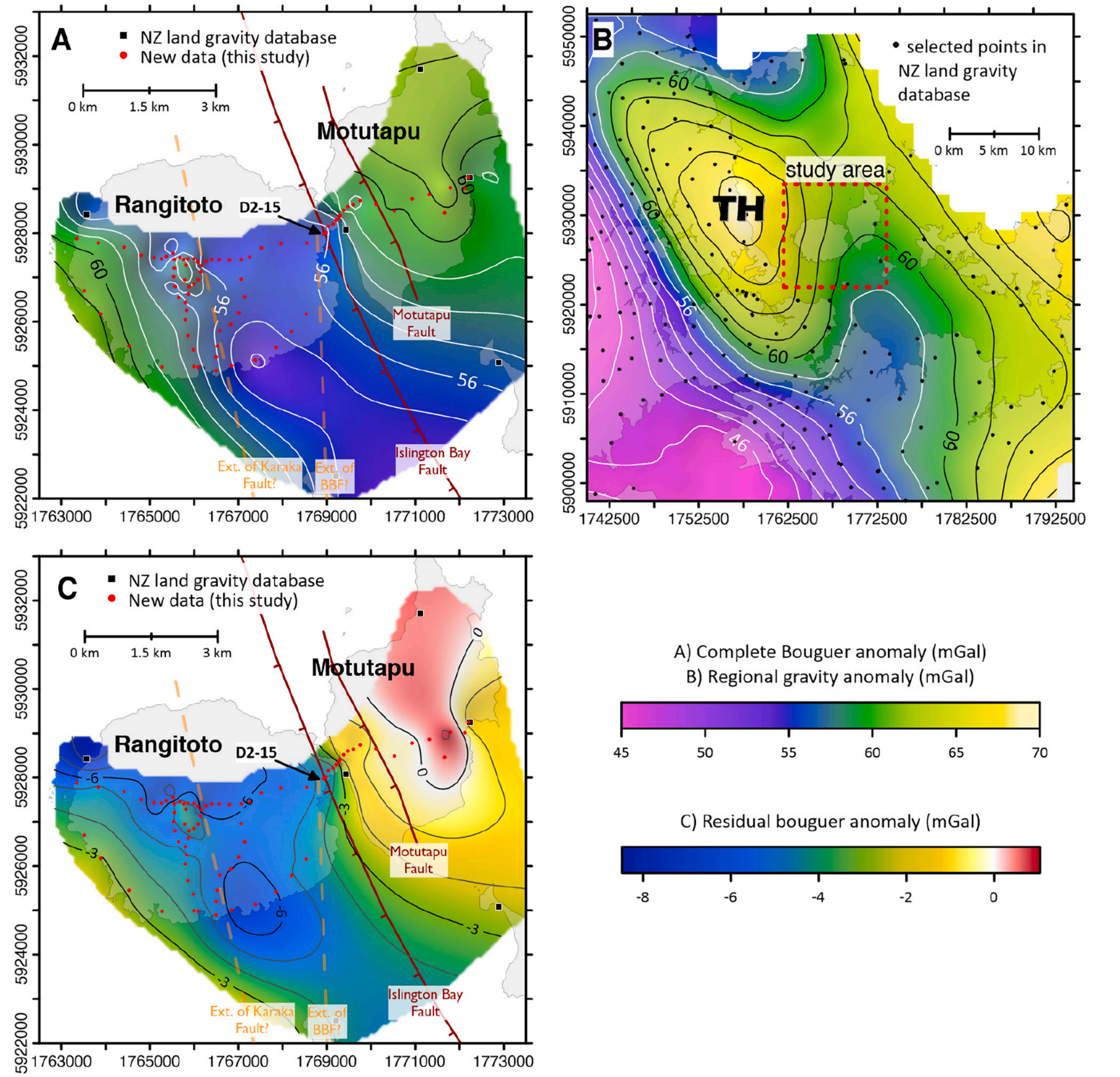

Fig. 3. (A) Complete Bouguer anomaly of the Rangitoto-Motutapu Islands, contour lines every 1 mGal. (B) Regional gravity anomaly of the Auckland Region extracted from (A), data from the New Zealand land gravity database excluding our new dataset (GNS Science, 2012; Stagpoole et al., 2021). Contour lines every 2 mGal, "TH" marks the Takapuna gravity high. (C) Residual gravity anomaly of the Rangitoto-Motutapu Islands, extracted from (A), with 1 mGal contour interval. In (A) and (C), BBF means "Bucklands Beach Fault.".

Cassidy and Locke, 2010). Flight line spacing varied between 250 and 1000 m (Eccles et al., 2005). Eccles et al. (2005) converted the raw aeromagnetic data to the total magnetic anomaly (or intensity, TMI) by removing the effects of diurnal variation, geomagnetic reference field, and random instrumental noise. Due to the lack of tie lines, no levelling correction was performed. Eccles (2003) estimated that the maximum uncertainty of magnetic data is ~ 8 nT, based on known instrumental and flight elevation uncertainties. Horizontal positioning uncertainty of the aeromagnetic survey is estimated to be ~ 3 –5 m (Eccles et al., 2005; Cassidy et al., 2007), which results in additional ~ 2 –4 nT uncertainty close to the centre of the Rangitoto magnetic anomaly.

The magnetic anomaly map (Fig. 4A) shows the influence of both Rangitoto volcano and eastern edge of the JMA to the southwest. The alignment of the Rangitoto magnetic anomaly dipole is NNE-SSW (~ 6°), within the range for Rangitoto basalt paleomagnetic declination (~ 350° to 13°; Shibuya et al., 1992; Robertson, 1986) and modelled 1450–1500 AD Rangitoto geomagnetic declination (~ 357° to 8°; Korte and Constable, 2011, Fig. 4C). Within the positive area of Rangitoto magnetic anomaly dipole are two peaks that align parallel to the Islington Bay Fault and nearby proposed Karaka Fault extension (Fig. 4A). The direction of 2001 AD geomagnetic field (DGRF epoch 2000; Alken et al., 2021, Fig. 4C) is still within the uncertainty ellipses of Rangitoto basalt paleomagnetic data (Fig. 4C). In the southern part of the map, a high magnetic anomaly is associated with Motukorea volcano (Fig. 4A).

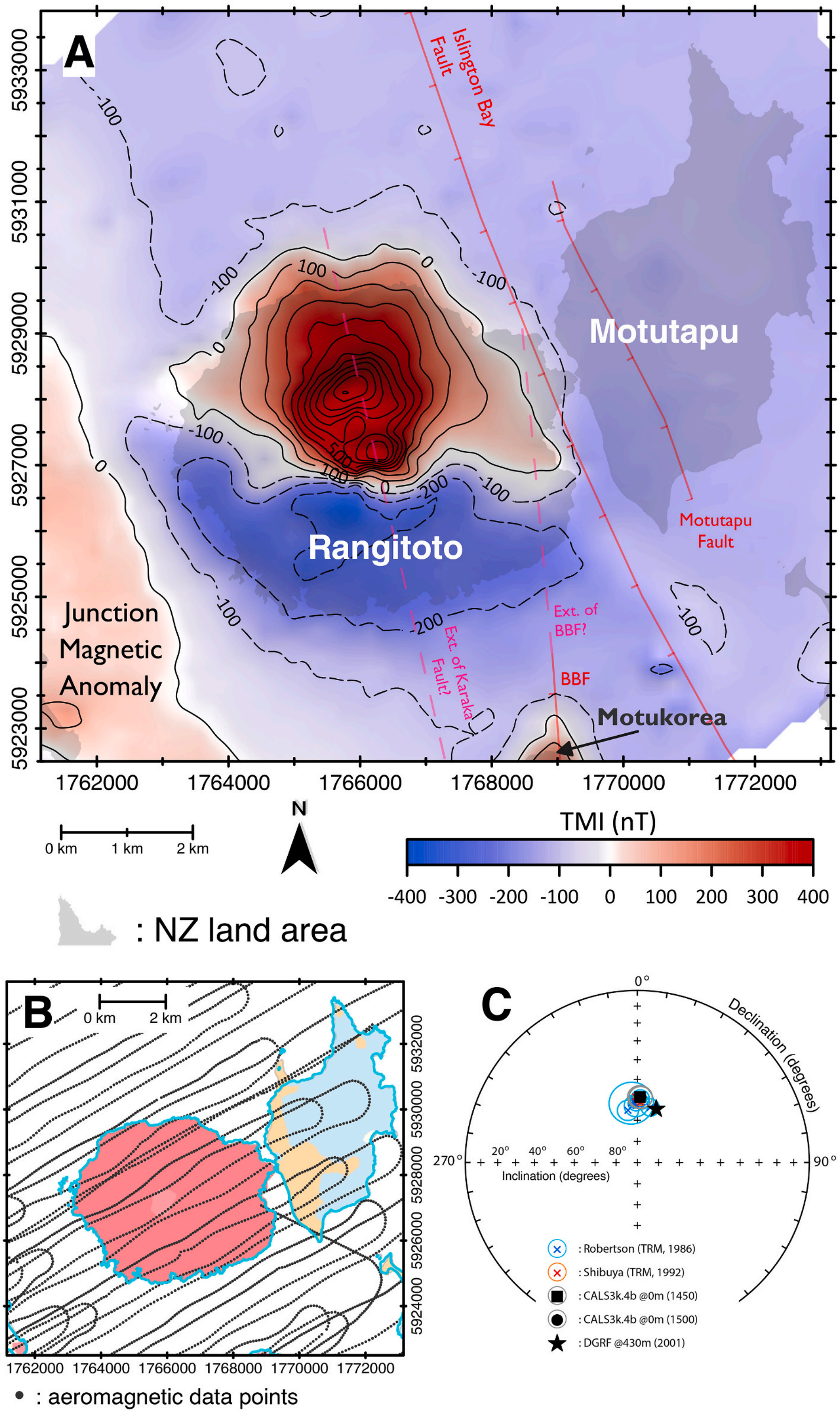

Fig. 4. (A) Magnetic anomaly map of the Rangitoto and Motutapu Islands. Contour lines every 100 nT, and BBF stands for Bucklands Beach Fault. (B) The location of the aeromagnetic data points, plotted on the geological map of Rangitoto and Motutapu. For colour legend, please refer to Fig. 1C. (C) Equal-area plot of Rangitoto basalt paleo-inclination and declination (acquired from thermoremanent magnetisation, TRM) with the modelled Rangitoto geomagnetic inclination and declination in 1450, 1500, and 2001 AD. The Rangitoto geomagnetic parameters for the year 1450 and 1500 AD are calculated on the earth surface using the CALS3k.4b model (Korte and Constable, 2011). DGRF epoch 2000 coefficients are used for calculating the 2001 AD geomagnetic parameters at 430 m above Rangitoto, the aeromagnetic flight level (Alken et al., 2021; Eccles et al., 2005). Paleomagnetic data is marked with cross, modelled values are marked with filled shapes, and 95% confidence ellipses are indicated. All inclination values are negative.

2.3. Regional and residual anomalies

A potential field anomaly can be separated into regional anomalies, typically having long spatial wavelength from deep-seated bodies, and residual anomalies which have short spatial wavelength sourced from bodies at or close to the surface. Thus, isolation of residual anomaly should be attempted for the investigation of Rangitoto volcanism. We computed the regional gravity anomaly from the New Zealand land gravity database covering the broader Auckland region (GNS Science, 2012, Fig. 3B), using a reduction density of 2.39 g/cm^3 with omission of data points located on Rangitoto and the western side of Motutapu. We gridded these data points with a 2 km cell spacing to produce a smoothly varying regional field. We acknowledge that absence of marine data points reduces the definition of regional gravity anomaly offshore. The regional gravity anomaly map generally shows gradually increasing anomaly values toward the east, connected by a low anomaly saddle with the Takapuna High (marked by "TH", Fig. 3B) on the northern part of the map. Rangitoto volcano is located at the southern side of this saddle (Fig. 3B). While higher regional gravity values in the eastern part of the map (Fig. 3B) are associated with basement outcrops, borehole data suggests depth to the basement near the Takapuna High is > 400 m (Fig. 1B) implying potential basement density heterogeneity (Williams et al., 2006).

We subtracted the regional map from the CBA to produce a residual gravity anomaly. The residual gravity anomaly map (Fig. 3C) shows a gravity high in the southwestern part of the map gradually changing into a broad area of low anomaly with troughs on the northern and southern part of Rangitoto. Moving east toward Motutapu, the broad low anomaly changes to a gravity high with a steep anomaly gradient at the inferred location of Islington Bay Fault (Kenny et al., 2012, Fig. 3C). Just like the CBA map (Fig. 3A), the residual map (Fig. 3C) shows a faint low gravity anomaly "ring" surrounding the elongate Rangitoto summit residual gravity high.

For the magnetic anomaly, we unsuccessfully experimented with regional-residual separation using various methods (upward continuation, moving average, gridding using equivalent sources/layers; Blakely, 1995). However, the similar spatial wavelength between the Rangitoto magnetic anomaly and the basement-sourced Junction Magnetic Anomaly to the west (Fig. 4A) proved challenging to separate. Hence, we analyse the total magnetic anomaly as shown in Fig. 4A and model both deep and shallow structures as required to fit the data.

2.4. Petrophysical data

Petrophysical data (rock density, magnetic susceptibilities, and remanent magnetisation) provides constraints for the modelling and interpretation of anomalies. Table 1 documents petrophysical data associated with samples of geological units that are exposed on, around, or hypothesised (Edbrooke, 2001; Linnell et al., 2016; Eccles et al., 2005; Ensing et al., 2022) to be present beneath Rangitoto. Units from the Dun Mountain-Maitai terrane are included as the probable source of the JMA seen in the southwestern corner of the study area (Figs. 1A and 4A).

All values in Table 1 came from laboratory measurements (PETLAB; Strong et al., 2016; Milligan, 1977; Robertson, 1986; Robertson, 1983, in SI). Eq. (1) below calculates the apparent susceptibility (χ_{app}, in SI) from the measured magnetic susceptibility (χ, in SI) and remanent magnetisation (M_R, in A/m) to make the units comparable for inversion modelling (Section 3). In calculating apparent susceptibility, we assume the direction of remanent magnetisation is close or similar to the inducing field **H**. Although Rangitoto basalt has a significant remanence (Konigsberger ratio > 1; Robertson, 1986), this assumption is valid because the directional difference between the Rangitoto basalt paleomagnetic and 2001 AD geomagnetic fields is within the uncertainty ellipse (Fig. 4C; Robertson, 1986; Shibuya et al., 1992). Thus, in Eq. (1), we can gain the 'remanent' component of the apparent susceptibility by dividing M_R with $|\mathbf{H}|$, the magnitude of the ambient magnetising field. According to DGRF epoch 2000 (Alken et al., 2021), $|\mathbf{H}|$ equals ~ 43.36 A/m at Rangitoto sea level in 2001 AD.

$$\chi_{app} = \chi + \frac{M_R}{|\mathbf{H}|} \tag{1}$$

The ultramafics of the Dun Mountain-Maitai terrane is another main main magnetic units that may present in our study area (Table 1; Eccles et al., 2005), which are Permian in age, significantly deformed, but are not exposed in situ in the AVF to constrain the unit's magnetic properties (Spörli et al., 2015). In this study, we assume that the Dun Mountain-Maitai Terrane is magnetised in the direction of the ambient geomagnetic field for simplicity. We define the "ambient geomagnetic field" as the DGRF epoch 2000 geomagnetic field 430 m above Rangitoto (total field 54354 nT, inclination -63°, declination 20°; Alken et al., 2021, Fig. 4C).

3. Modelling the subsurface structure of Rangitoto

3.1. Modelling approach

We implement 2.5D and 3D modelling techniques to investigate the location of crustal heterogeneities and structures within Rangitoto volcano and the basement using the gravity and magnetic data. We undertake forward 2.5D modelling (Talwani et al., 1959; Talwani and Heirtzler, 1964) implemented in the GM-SYS module of Oasis Montaj (Seequent Limited, 2020), for an west-east transect across Rangitoto and Motutapu Islands and a north–south transect through the Rangitoto summit. Independent 3D inverse modelling using SimPEG is also performed (Cockett et al., 2015). Overall model fit is expressed as a root mean square error (RMSE) value.

In 2.5D modelling, 2D geophysical bodies extend a defined distance (2.5 km, the approximate radius of Rangitoto Island) in and out of the model plane, and each model unit has homogeneous magnetisation and density properties. Physical property and topographic variations in the direction perpendicular to the profile line are not accounted for in 2.5D models, and this is expected to lead to two issues: overestimation of the modelled gravity and magnetic effects or underestimation of the density contrast, and issues with making an exact match between perpendicular profiles using the same DC shift. This shortcoming is addressed by the 3D modelling.

Potential field modelling is well known for its non-uniqueness problem, where multiple different models can reproduce the same anomaly (e.g., Skeels, 1947; Rosas-Carbajal et al., 2017). We mitigate this problem through the incorporation of physical properties and geometric constraints in the modelling process. Physical property limits in both modelling procedures honour the petrophysical data shown in Table 1. Independent geometric constraints from surface geology and drill hole logs are also used to reduce ambiguity in the gravity and magnetic data modelling. The surface geology is informed by published geological maps (Kermode, 1992; Edbrooke, 2001; GNS Science, 2020,

Table 1
Petrophysical properties of samples from relevant geological units. Superscripts refer to: 1. PETLAB database (Strong et al., 2016), 2. Milligan (1977), and 3. Robertson (1983), Robertson (1986). Number of samples is given by N. When calculating the apparent magnetic susceptibility column, absent magnetic susceptibility data is assumed to be zero. See Supplementary Material 3 for individual sample information.

Geological Units	Wet Density (g/cm^3)	Measured Susceptibility (SI)	Remanent Magnetisation (A/m)	Apparent Magnetic Susceptibility (SI)
Rangitoto basalt[2,3]	2.535 ± 0.207; N = 59	0.002–0.038; N = 25	2.440–46.88; N = 58	0.064–1.085; N = 58
Rangitoto tephra and scoria[2]	1.630–2.400; N = 7	Data not available	1.020–37.14; N = 5	0.024–0.860; N = 5
Waitemata Group sandstone and mudstone[1,2]	2.255 ± 0.201; N = 17	< 0.01; N = 11	Not measured	Not calculated
Waipapa Terrane greywacke[1,2]	2.655 ± 0.094; N = 50	< 0.004; N = 19	Not measured	Not calculated
Dun Mountain-Maitai terrane peridotite (partly serpentinised)[1]	3.081 ± 0.254; N = 76	0.001–0.062; N = 44	0.060–4.770; N = 7	0.001–0.113; N = 44

Fig. 1A). Drill hole logs are lodged in PETLAB (Strong et al., 2016) and the New Zealand Geotechnical Database (EQC, 2012, see their locations in Fig. 1B). The thickness and physical properties of known geological units are respected and tied together at the point where the west-east and north–south transects cross. As the north–south profile is parallel to the basement-offsetting Islington Bay Fault and JMA, a differential static shift is allowed as the 2.5D modelling cannot account for their expected regional gravitational and magnetic effects. Remaining model uncertainties are acknowledged by demonstrating two geologically possible model endmembers with closely similar fits to the data.

For total magnetic anomaly modelling, we assumed that all model units are magnetised in the direction of the ambient geomagnetic field. As such, we modelled the magnetic anomaly using apparent susceptibility instead of solving for full magnetic vectors. The full vector modelling of magnetic anomaly data increases model ambiguity and requires additional regularisation compared with a simple susceptibility modelling where the magnetisation direction is fixed (e.g., Fournier et al., 2020).

3.2. 2.5D models of Rangitoto

We applied some geological simplifications in making the 2.5D models. For example, drill hole logs (Linnell et al., 2016; Strong et al., 2016) indicate that local Quaternary sediment thickness is volumetrically insignificant (< 100 m thick) to cause a resolvable gravity anomaly. Thus, we combine the unit with Waitemata Group into one Cenozoic sediment unit in 2.5D gravity models. In 2.5D magnetic models, we further combine the Cenozoic sediment and the Waipapa metasedimentary basement into one magnetic unit, assigned with 0 SI apparent susceptibility value. We base this decision on the negligible

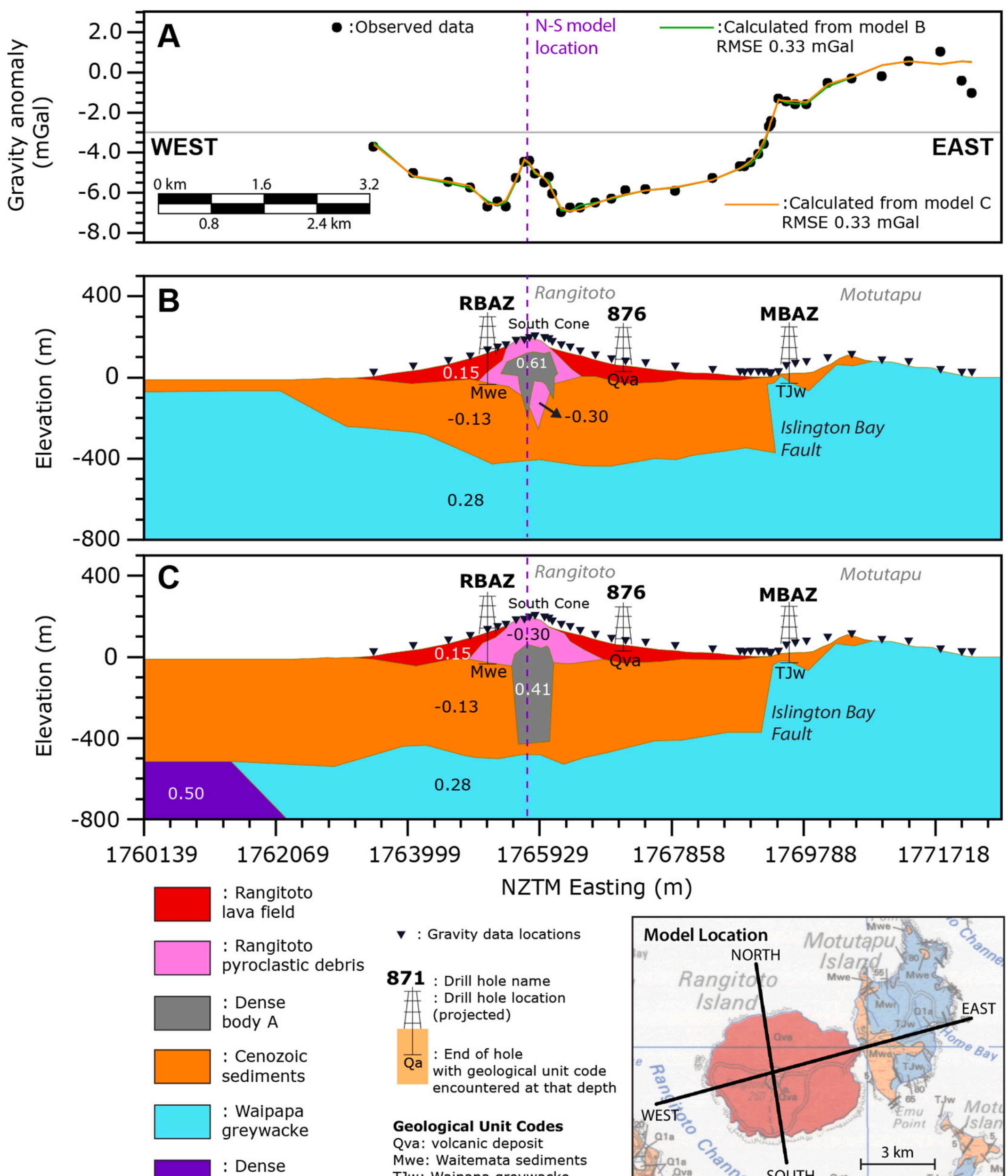

Fig. 5. (A) Observed and calculated gravity anomaly data of west-east Rangitoto to Motutapu Islands transect. The grey line marks −3 mGal. (B) and (C) are two endmembers of the 2.5D models of subsurface density distribution below the transect. Density contrasts are relative to 2.39 g/cm^3 reduction density. The legend and locator map for the models are below (C). Offline wells and data point elevations have been projected onto the 2D topographic surface shown.

susceptibility values of both the Waitemata Group and Waipapa Terrane greywacke (Table 1).

3.2.1. West-east Rangitoto to Motutapu Island transect

In this transect, the broad residual gravity low over Rangitoto can be fitted with lower density material associated with the scoria cone overlying thick (~ 500 m) Cenozoic sediments (Fig. 5). Increasing gravity to the West is potentially from an imperfect regional field removal and can be linked to a shallowing basement or, to be consistent with sediment thickness from boreholes west of Rangitoto (Fig. 1B, also see par. 1 in Section 2.3), a deeper high density basement body ("dense body B", Fig. 5C).

Fitting the small gravity high at Rangitoto summit requires a dense body within the cone complex ("dense body A", Fig. 5). We modelled the sub-cone dense body to have a density contrast of 0.41 –0.61 g/cm^3 (Fig. 5), which corresponds to an absolute density of 2.8 –3.0 g/cm^3, possibly consistent with low-vesicularity basalts (e.g., Johannes and Smilde, 2009) but relatively denser compared to the measured density of surficial Rangitoto basalt (Table 1). When the sub-cone dense body has lower density contrast (0.41 g/cm^3), it will be deeper (~ 150 m below summit) and larger (~ 600 m width, 480 m high, Fig. 5C). At higher density contrast (0.61 g/cm^3), the sub-cone dense body will be shallower

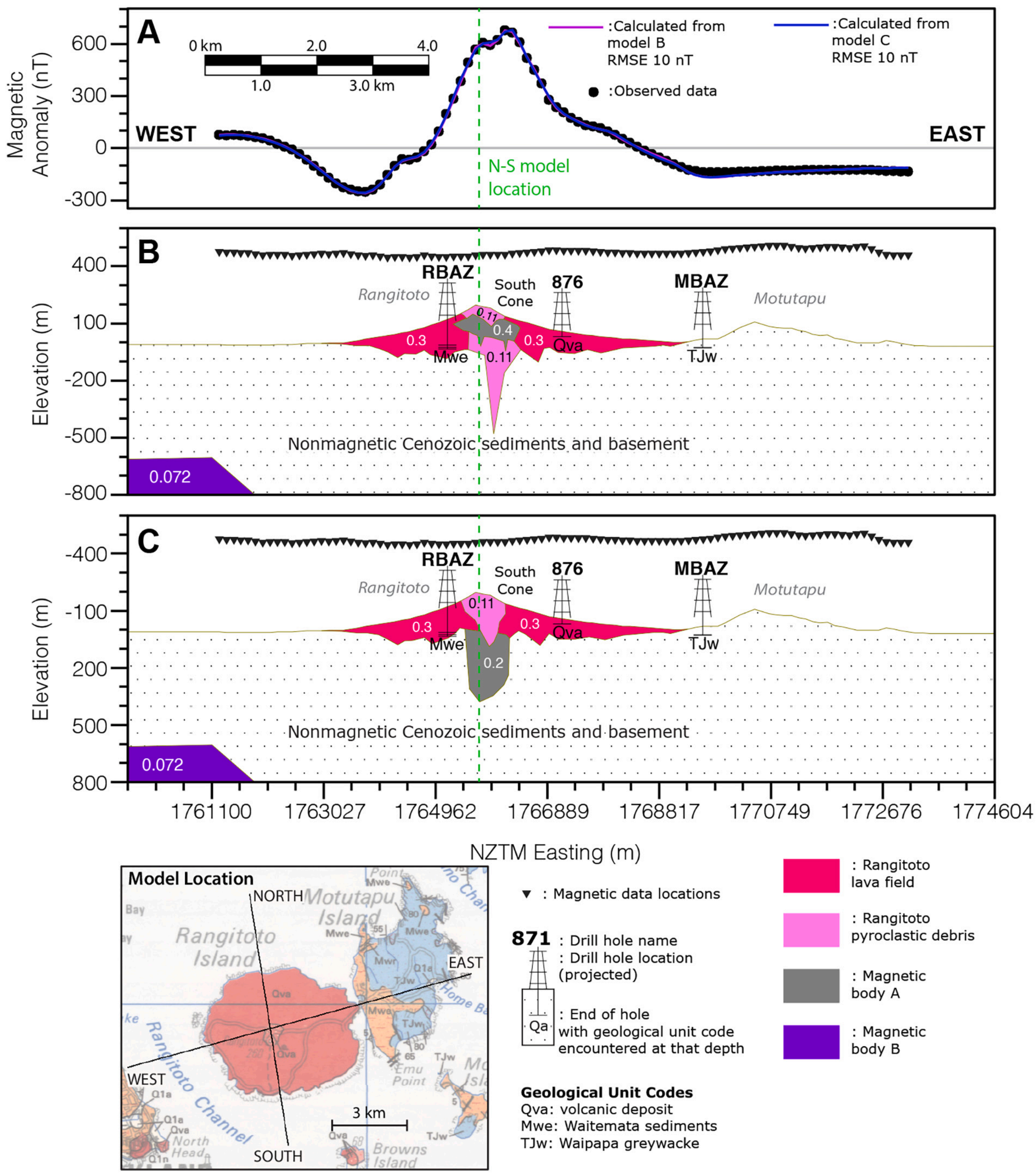

Fig. 6. (A) Observed and calculated magnetic anomaly data of west-east Rangitoto to Motutapu Islands transect. Grey line marks 0 nT. (B) and (C) are two end-members of the 2.5D models of subsurface susceptibility distribution below the transect. Legend and locator map to the models are below (C). True offline well and data point elevations have been projected onto the 2D topographic surface shown.

(~ 70 m below summit) and smaller (e.g. ~ 800 m width, 160 m high, Fig. 5B).

Modelling the Islington Bay Fault as a step in Cenozoic sedimentary thickness fits the rapidly increasing gravity anomaly east of Rangitoto (Fig. 5). The step can take the form of a reverse (Fig. 5B) or a more geologically likely (Edbrooke, 2001) normal fault (Fig. 5C), both are steeply dipping (> 60°) and fit the data equally. The shallow basement east of the Islington Bay Fault is consistent with the MBAZ drillhole logs showing only 90 m of Waitemata Group. The Cenozoic sediments then continue to thin across Motutapu Island, as shown by basement outcrops in valleys on the island (Edbrooke, 2001). Our 2.5D west-east gravity models (Fig. 5) do not require step-like features associated with the potential extensions of the Karaka and Buckland Beach faults (see Fig. 3 for locations) although such basement topography could trade-off with near-surface volcanic structures.

Magnetic anomaly data on the west-east Rangitoto-Motutapu transect (Fig. 6A) show a prominent dipole anomaly associated with Rangitoto volcano. The majority of the magnetic anomaly can be fitted using apparent magnetic susceptibilities of 0.26 to 0.33 SI for the Rangitoto lava field on the volcano flanks (Fig. 6). However, to account for the central magnetic anomaly peak, a concealed magnetic body ("magnetic body A") is required in or beneath the low susceptibility (0.11 SI) scoria cone (Fig. 6). This magnetic body occupies a similar location to the high density body in gravity models (Fig. 5). Like the sub-cone high-density

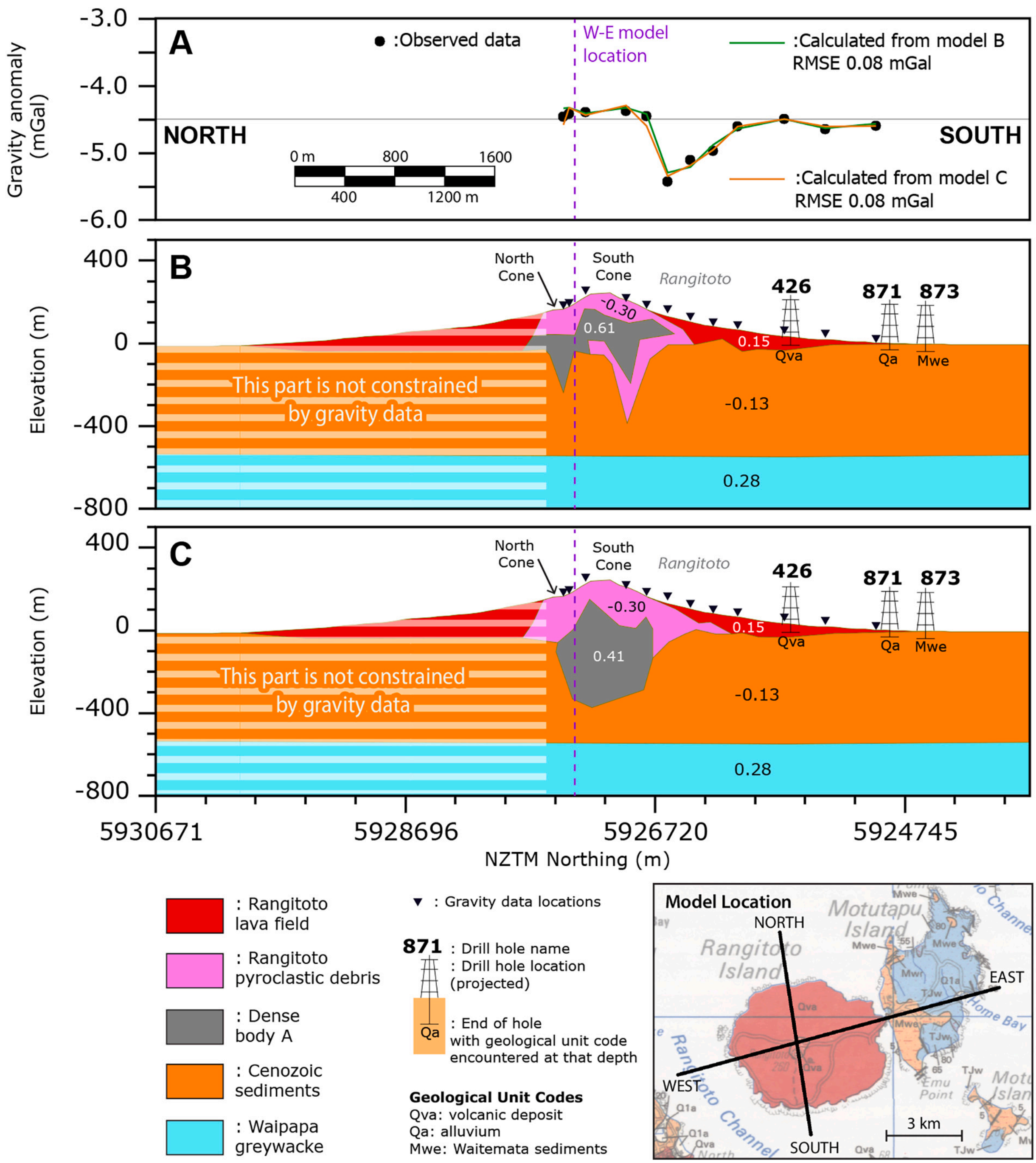

Fig. 7. (A) Observed and calculated gravity anomaly data for the north–south Rangitoto flank transect. The grey line marks −4.5 mGal. (B) and (C) are two endmembers of the 2.5D models of subsurface density distribution below the transect. Density contrasts are relative to 2.39 g/cm^3 reduction density. The legend and locator map for the models are below (C). True offline wells and data point elevations have been projected onto the 2D topographic surface shown.

"body A" in the W-E gravity model (Fig. 5), higher susceptibility requires the sub-cone magnetic body to have smaller geometry coupled with shallower depth (cf. Fig. 6B & C). The depth of the sub-cone magnetic body ranges from ~ 70 m to 200 m below topographic surface, with shape ranging from a 1250 m wide, 100 m high sill-like body up to 800 m wide, 380 m high vertically elongate body (Fig. 6). On the western side of the profile, "magnetic body B" with 0.072 SI apparent susceptibility is needed to fit the anomaly data (Fig. 6).

3.2.2. North–south Rangitoto transect

The north–south Rangitoto transect, covered by gravity anomaly data only from the South Cone southward (Fig. 7A), shows a 0.7 km-wide, 1 mGal negative anomaly just south of the South Cone. This location does not correlate with the mapped low density scoria cones (c.f. Figs. 7 & 1A; Table 1); instead, we can consider two flanking highs as the cause of the 'relative' low. To the north, a dense body with density contrast of $0.41-0.61\ \mathrm{g/cm^3}$ ("dense body A", Fig. 7) is required inside or beneath the cones, and to the south is the basaltic lava field with $0.15\ \mathrm{g/cm^3}$ density contrast. Similar to the west-east transect, a higher

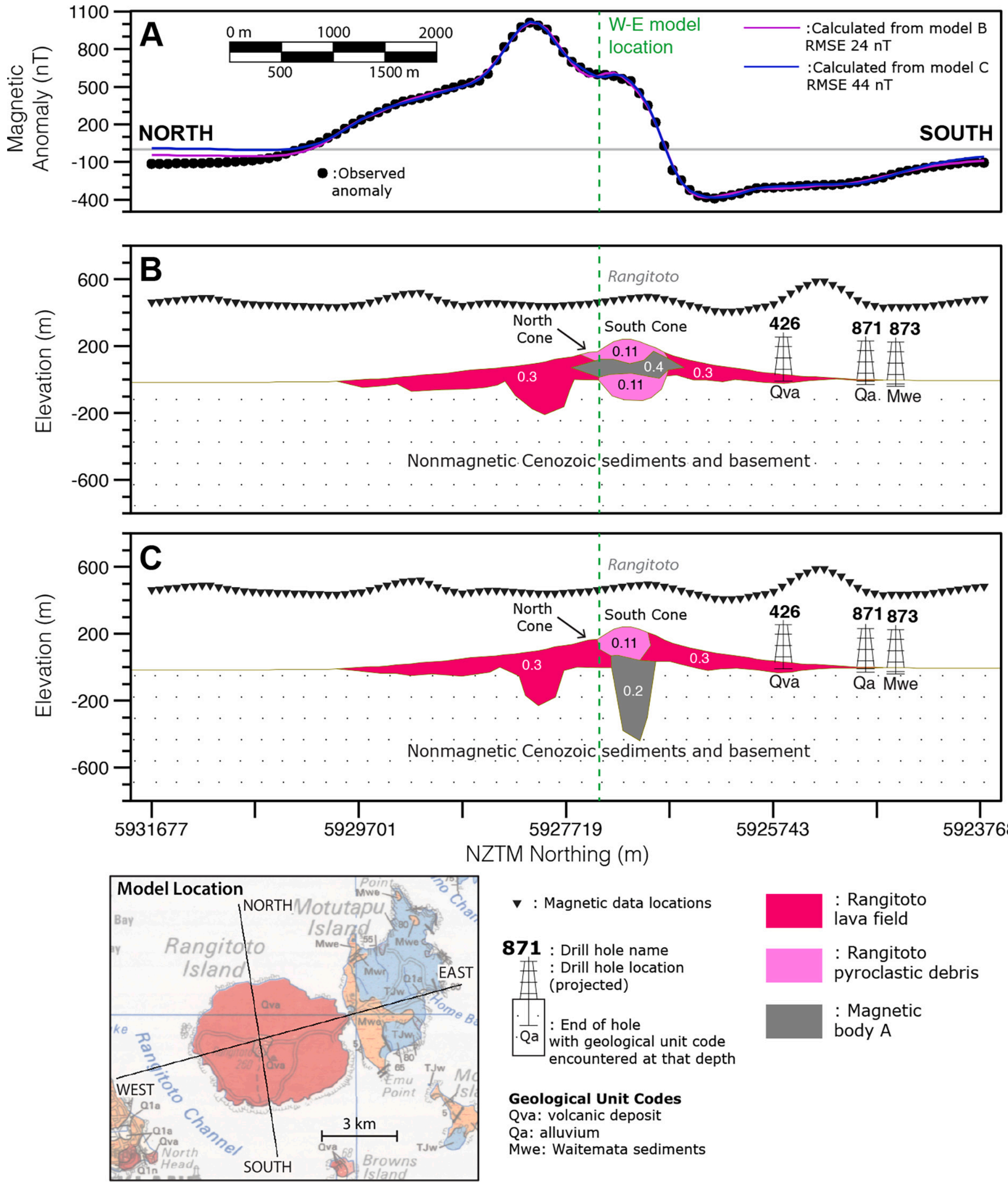

Fig. 8. (A) Observed and calculated magnetic anomaly data of north–south Rangitoto Island transect. Grey line marks 0 nT. (B) and (C) are two endmembers of the 2.5D models of subsurface susceptibility distribution below the transect. Legend and locator map to the models are below (C). True offline well and data point elevations have been projected onto the 2D topographic surface shown.

density sub-cone body will make its depth shallower and size smaller (Fig. 7A). The depth of the sub-cone dense body can range from $\sim$ 50 to $\sim$ 200 m below the topography, with shapes either thin and horizontal or thicker and vertically oriented (Fig. 7B & C). The northern limit of the sub-cone dense body can not be fully constrained from the current gravity data coverage.

The Rangitoto magnetic anomaly (Fig. 8A) captured on the north–south transect exhibits a dipolar nature. Most of the anomaly is accounted for by a 0.3-SI unit on the flanks for the volcano (Fig. 8). To fit the anomaly peak correlated with what we interpret as less magnetic (0.11 SI) scoria cones, a concealed high susceptibility body is required (Fig. 8B-C). With a lower susceptibility value, this body will be larger and buried (Fig. 8C). The high susceptibility body can be a 500-m high, 470-m wide 0.2 SI rectangular body (Fig. 8C), or a 160-m thick, 1.2-km wide 0.4 SI sill-like body (Fig. 8B).

Just north of the central scoria cone, over the lava field, is the highest amplitude magnetic anomaly peak (Fig. 8A). Absence of independent geological or gravity data in that area causes us to model conservatively with thickened magnetic material (0.3 SI; equal to the lava field) with a V-shape, width of $\sim$ 410 m and thickness approximately 170 to 220 m.

3.3. Three dimensional models of Rangitoto

Two-and-a-half dimensional modelling indicates that the presence of a dense, magnetic body beneath Rangitoto scoria cones is required, assuming the scoria cones are homogeneously low density and susceptibility. The 2.5D gravity model also indicates a step in Cenozoic sediment thickness at the location of the Islington Bay Fault, however the Motutapu Fault is not associated with a discernible gravity signature. In this section, we test the robustness of these structures in 3D gravity and magnetic models.

In 3D gravity and magnetic inverse modelling with SimPEG (Cockett et al., 2015), the earth is divided into volume elements, or voxels. Accepting that the gravity data distribution is still approximately 2D along two perpendicular transects, and realising that the 3D model is most reliable along these transects, the gravity model voxel size has been chosen and tested, scaled based on the gravity station spacing (e.g., Trevino et al., 2021; Miller et al., 2017). Meanwhile, aeromagnetic data provides better coverage over the entire islands, and the voxel size is scaled based on the flight-line spacing (e.g., Miller et al., 2020) and tested. All voxels in the model are embedded within an octree mesh, which allows refinement of the mesh around topography and data points, called the core mesh. This core mesh extends to 1000 m depth and is padded with increasingly larger cells out to 6 km from the edge of the data to capture long wavelength and edge effects.

In the inversion set up we pre-set the data uncertainty, physical property bounds, and regularisation norms to tailor the inversion to our requirements. Optimum data uncertainty is chosen by visual inspection of models and convergence curves so the inversion will not underfit or overfit the data. At higher uncertainty values, the inversion underfits the data evident from the large difference between observed and modelled data, or high residuals (UBC-GIF, 2018a). Lower uncertainty value leads to overfitting, leading to spurious, small scale structures in the model (UBC-GIF, 2018a). Property bounds are the limits of magnetic susceptibility and density property value that can be taken by the voxels, and are determined based on Table 1. The regularisation controls the distribution of the amplitude and gradient of physical property in the voxels, creating smoother or more compact models (UBC-GIF, 2018b). Stopping criterion for the inversion process is determined by the minimum misfit parameter as well as a minimum change ($\leq 10^{-4}$) in the objective function between successive iterations. The inversion sets the minimum misfit parameter to half the number of data points, assuming that the misfit follows a chi-square distribution with chi-factor equals 1.

For this study, we vary the model norm regularisation parameter to produce the smooth and compact endmembers of the model. The model norm is expressed as a mixed ℓ_p −norm(p, $q_{x,y,z}$), where the p-norm controls the physical property amplitude and q-norm controls the physical property gradient in x, y, and z directions (Fournier and Oldenburg, 2019). The value of p-norm and q-norm spans from zero to two (Fournier and Oldenburg, 2019). At $p, q_{x,y,z} = 0$, the inversion produces a compact sparse model where most model values are set to 0 and the minimum number of model cells are set to a high contrast value (Miller et al., 2020; Trevino et al., 2021). Meanwhile at p, $q_{x,y,z} = 2$, the inversion attempts to have minimum change between cells, resulting in generally smooth models with lower amplitude cell values across the model space (Miller et al., 2020; Trevino et al., 2021). The inversion starts with a homogeneous half-space of 10^{-4} model units.

3.3.1. Gravity model

The 3D gravity model of Rangitoto (Fig. 9) is constructed on an octree mesh with a core cell size of $50 \times 50 \times 10$ m. By visual inspection of a range of models, with different uncertainty values, we choose 0.2 mGal as our preferred uncertainty value. Next, we set the density contrast bounds at $-0.3\ \mathrm{g/cm^3}$ (lower bound) and $0.6\ \mathrm{g/cm^3}$ (upper bound) respectively, relative to the reduction density ($2.39\ \mathrm{g/cm^3}$). These bounds cover the limits of our petrophysical samples (Table 1) and the density used by 2.5D models (Figs. 5 and 7). We then run the inversion for compact and smooth endmembers, represented by $(0, 2, 2, 2)$ and $(2, 2, 2, 2)$ model norms, respectively. The inversion runs for a maximum of 30 iterations, which the compact endmember (Fig. 9A,C,E) used up to completion. On the other hand, the smooth endmember (norm $= 2, 2, 2, 2$; Fig. 9B,D,F) stopped at iteration 20 as it reached the minimum permissible change in objective function value.

Both endmember 3D gravity models show the presence of a high-density body (density contrast $>\sim 0.1\ \mathrm{g/cm^3}$) below the South Cone, surrounded by a lower density (density contrast $< -0.05\ \mathrm{g/cm^3}$) body to its west and east (Fig. 9A and B). The north–south section shows that this high density body is wider in this orientation (Fig. 9C–D), and vertical slices at 79 m below sea level (Fig. 9E–F) also indicates that body is elongated NW-SE, parallel to the Islington Bay fault and hypothetical Karaka Fault extension. East of Rangitoto, only the Islington Bay Fault is resolved unambiguously by both model endmembers (Fig. 9A & B). No discernible density contrasts associated with the Motutapu Fault, or extensions of Karaka and Bucklands Beach Fault can be identified in the 3D gravity model slices (Fig. 9).

3.3.2. Magnetic model

Because of differences in data acquisition characteristics, we use a different mesh for the 3D Rangitoto magnetic models. The magnetic models (Fig. 10) use an octree mesh with core cell size of $100 \times 100 \times 25$ m. Visually inspecting models produced by various data uncertainty values (from 8–20 nT) led us to choose 10 nT as the optimum uncertainty value, close to the total uncertainty of magnetic data from all accountable sources (see Section 2.2). Physical property bounds are set between 0 and 0.5 SI to match our petrophysical data and 2.5D model physical property limits. Endmember models are created using $(0, 1, 1, 1)$ and $(2,2,2,2)\ell_p$-norms. We choose a more compact endmember $(0, 1, 1, 1)$ compared to the gravity data $(0, 2, 2, 2)$ because of better magnetic data coverage allowing us to exploit the data a little further. We allow 60 iterations for 3D magnetic modelling since magnetic inversions may converge slower than the gravity ones, which again used up by the compact endmember (Fig. 10A,C,E) to completion. Meanwhile, the smooth $(2, 2, 2, 2)$ endmember (Fig. 10B,D,F) stopped at iteration 15 as it reached the minimum permissible change in objective function value.

The 3D magnetic models from the compact (Fig. 10E) and smooth (Fig. 10B, D, F) endmembers are consistent with each other. The general feature is a central, vertically elongated magnetic body below the Rangitoto summit that branches into two at depths shallower than $\sim$ 250 m (Fig. 10A–D). In the horizontal depth slice made at 81 m below sea level (Fig. 10E–F), it becomes clear that those branches are parts of high ($>$ 0.1 SI) apparent susceptibility zones at the South Cone (labelled

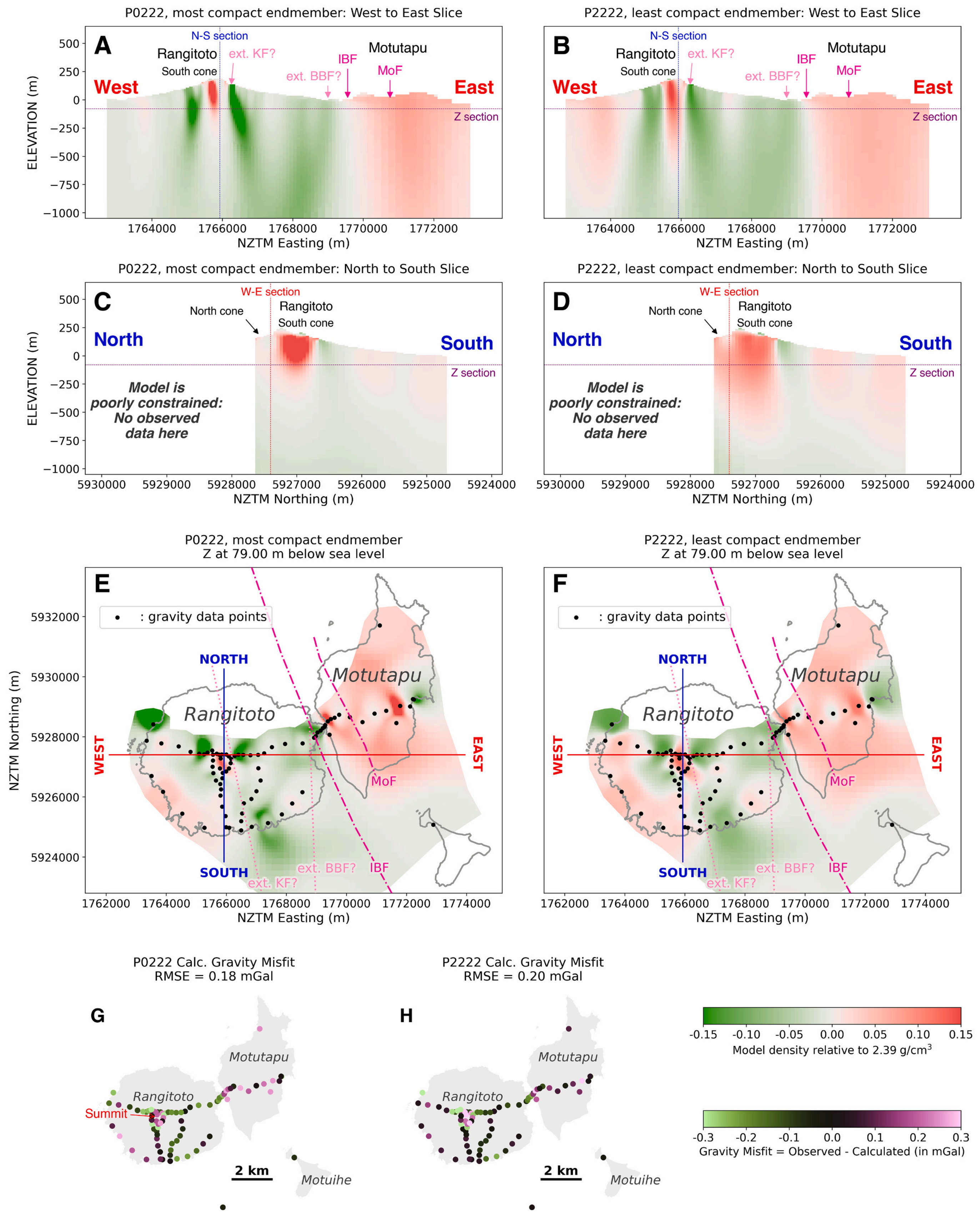

Fig. 9. 3D gravity model of Rangitoto subsurface. Figures (A, C, E) represent the west-east, north–south, and vertical slices of compact endmember (p-norm = 0) of the gravity 3D models. Vertical slice is made at 79 m below sea level. Compare figures (A, C, E) with figures (B, D, F) from the smooth (p-norm = 2) gravity model endmember. Figures (G) and (H) are the data misfit maps of the compact and smooth models, respectively. IBF: Islington Bay Fault, MoF: Motutapu Fault, ext. BBF?: extension of Bucklands Bay Fault (uncertain), ext. KF?: extension of Karaka Fault (uncertain).

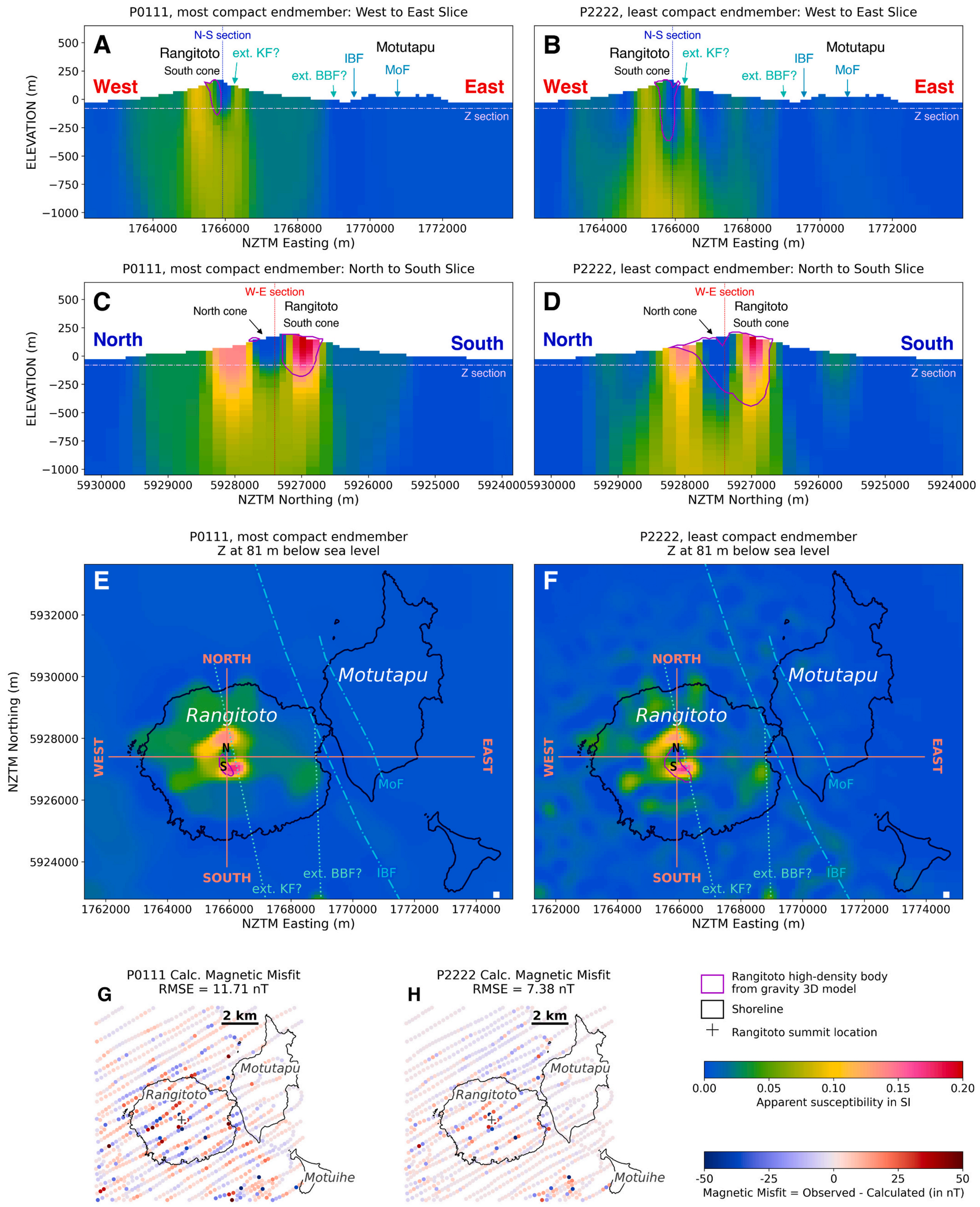

Fig. 10. Three-dimensional magnetic model of Rangitoto subsurface. Figures (A, C, E) show the west-east, north–south, and vertical slices of compact endmember $[0, 1, 1, 1]$ of the gravity 3D models. Vertical slice is 81 m below sea level. Purple line delineates part of the 3D gravity model with $> 0.035\ \mathrm{g/cm^3}$ density contrast. Compare figures (A, C, E) with figures (B, D, F) from the smooth $[2, 2, 2, 2]$ magnetic model endmember. North and South cones of Rangitoto are marked with N and S in figures E and F. Figures (G) and (H) are the data misfit maps of the compact and smooth models, respectively. IBF: Islington Bay Fault, MoF: Motutapu Fault, ext. BBF?: extension of Bucklands Bay Fault (uncertain), ext. KF?: extension of Karaka Fault (uncertain).

'S' in Fig. 10F) and just north of the North Cone (labelled "N" in Fig. 10E–F). These localised high apparent susceptibility zones are aligned parallel to the Islington Bay Fault and nearby hypothetical extension of Karaka Fault (Fig. 10E–F). Below the South Cone, the location of high susceptibility voxels coincides with the high density voxels in the 3D gravity model (Fig. 10C–F). That high-density body also extends out toward the low susceptibility region in smooth model end-member (Fig. 10B, D, F) which may be due to the effect of the smooth model regularisation, poor gravity data coverage at the northern flank of Rangitoto, or both.

4. Discussion

The analysis and modelling performed have enabled us to gain three main insights into the subsurface density and magnetisation structure of Rangitoto and Motutapu. First, gravity and magnetic models show that a dense and high susceptibility body is required beneath the Rangitoto scoria cones to account for the observed anomalies. The second is that the gravity models (Figs. 5 & 9) also provide an estimate on the geometry of the Islington Bay Fault, a major basement structure. However, other mapped basement structures like Motutapu Fault are not resolved, maybe due to limited vertical offset of contrasting materials and low gravity resolution from a reduced number of stations in this area. Potential northward extensions of Karaka and Bucklands Beach faults are also not resolved (Fig. 9A–B) either because the offsets of contrasting materials at these faults are too small to generate resolvable gravity signals, or that they do not continue below the model profile (Fig. 9E–F). Previously, the role those faults play in the formation of Rangitoto can only be inferred from topographic and vent lineament (Hayward, 2019). Now, new magnetic models (Fig. 10) provide the third insight that another high-susceptibility body exists north of the North Cone. This body is in a N-S alignment with both the North and South Cones of Rangitoto, supporting our hypothesis of structural control on Rangitoto eruption even further.

Although 2.5D and 3D models used for estimating the subsurface Rangitoto structure are broadly in agreement, they have their strengths and limitations. Two-and-a-half dimension forward models (Figs. 5–8) are excellent for detailed exploration of possible subsurface geology, allowing precise placement of bodies and boundaries not affected by model cell size or regularisation. However, their geometrical assumption (see Section 3.1) is only valid for regional structures that extend beyond the study area with offsets exceeding topographic variations, such as the Islington Bay Fault. This assumption is less suitable for evaluating Rangitoto volcanism-related bodies, which are bounded in three dimensions. The unsuitability of the 2.5D modelling assumption is evident in the high geometrical uncertainty of dense, high susceptibility body under the South Cone in 2.5D models (Figs. 5–8), which is very sensitive to change in the physical property value. In 3D models, the geometrical extent of the same body is stable across endmembers (Figs. 9 and 10), despite the inversion being set to fill the voxels with any physical property value within the limits similar to the 2.5D models (see Section 3.3). However, without additional constraints, 3D inversion tends to fit high-frequency anomalies with high physical property values in voxels close to the surface (UBC-GIF, 2018c). This can be seen in the north–south transect, where the 3D models shows a dense, high-susceptibility body directly under the southern flank of South Cone (Figs. 9 and 10) compared to the 2.5D models, where we put this body deeper to match the mapped geology (Figs. 7 and 8).

4.1. The plumbing system of Rangitoto

A number of studies have proposed how the Rangitoto eruption progressed (Needham et al., 2011; Hayward, 2017; Linnell et al., 2016) to construct the present-day landform. Hayward (2017) conceptualises Rangitoto as composed of central, multilayered scoria cones standing above an older tuff ring, both surrounded by a lava field. However, modelling of gravity and magnetic data (Figs. 5–10) found that a high-density magnetic body is required within or below the low-density, low-magnetic susceptibility scoria cones, which was not present in any prior model. We interpret this body to consist of low vesicularity and solidified basaltic intrusion.

Three-dimensional gravity and magnetic models consistently show that a dense, high susceptibility body, interpreted as a basaltic mass is present under the South Cone at $<$ 300 m depths, although with a slightly different horizontal extent (Figs. 9 and 10). In vertical cross-sections, the shape of the South Cone dense body is more elongate and fault-parallel (Fig. 9E and F) than the South Cone high-susceptibility body, which is more circular (Fig. 10E and F). Differences in density, distribution, and acquisition elevation between gravity and magnetic data, and model cell size likely account for small differences in the mass geometry. In the 2.5D models (Figs. 5–8) this feature is resolved as a dense, magnetic body A below the Rangitoto scoria cones.

In 3D gravity models (Fig. 9), the elongate shape and shallow depth of the South Cone basaltic mass suggest that it might be a solidified intra-cone feeder dyke (Fig. 11) instead of a feeder pipe or bulb-shaped lava lake. The feeder pipe interpretation, deduced from the vertical slices of 3D magnetic models (Fig. 10E–F), is weaker since the magnetic method is less sensitive than the gravity method in differentiating the denser feeder dyke from the more porous Rangitoto volcanic material, both can be magnetised equally strongly (see Table 1). Moreover, the circular shape of the South Cone high-susceptibility body could come from the blurring of the magnetic anomaly signal effected by the acquisition elevation ($\sim$ 430 m; Eccles et al., 2005). Interpreting the South Cone basaltic mass as a feeder dyke instead of a bulb-shaped lava lake, represented by the shallow, dense, magnetic body under the scoria cones in 2.5D models (panel B of Figs. 5–7), is also preferable because a bulb-shaped lava lake would give a circular-shaped Rangitoto summit gravity high instead of an elongate one like in Fig. 3. Intra-cone feeder dykes have been observed in outcrops from small-volume volcanic fields worldwide (e.g., Houghton and Schmincke, 1989; Petronis et al., 2013; Carracedo-Sánchez et al., 2017). Nevertheless, the modelled width of the South Cone basaltic mass (Fig. 9) is up to 2 orders of magnitude wider than intra-cone dyke outcrops associated with small-volume volcanic fields (Petronis et al., 2013; Houghton and Schmincke, 1989), which we attribute to modelling resolution ($50 \times 50 \times 10$ m cell size) and regularisation effects.

Three dimensional magnetic models (Fig. 10) also suggest that another high susceptibility body exists north of the North Cone. In the 2.5D model (Fig. 8) this body correlates to the V-shaped body north of the North Cone. Absence of additional geological and gravity information north of the North Cone makes it harder to interpret the volcanological significance of this body. We hypothesise that the high-susceptibility body beneath the lava field north of the North Cone might be associated with a buried conduit or thickened lava pile (Fig. 11A). The northern and South Cone high-susceptibility bodies of Rangitoto are separated by a zone of low susceptibility ($\sim$ 0 SI) associated with the North Cone tephra (Fig. 10).

North–south vertical slices of 3D magnetic models (Fig. 10C-D) shows that at $>$ 250 m depth, the northern and South Cone high ($\geqslant$0.065 SI) susceptibility bodies merge into a single body of $\sim 0.065-0.070$ SI apparent susceptibility. In the 2.5D models, this body is relevant to the elongate, deeper seated dense, magnetic body under the scoria cones in the panel C of Figs. 5–8. While the elongate high susceptibility ($\geqslant$0.065 SI) bodies in this slice can be interpreted as a solidified basalt magma pathway (see Table 1), the merger itself can be interpreted in two ways. First is that a single magma conduit has actually bifurcated in the near-surface from a single pathway, or secondly that the models simply fail to resolve closely-separated parallel magma pathways due to decreased model resolution with depth. The first interpretation implies that there was magma pathway reuse during Rangitoto lifetime. We consider this less likely since the $\sim 30-60$ years gap between individual Rangitoto eruptions is long enough for subvolcanic feeder dykes to solidify

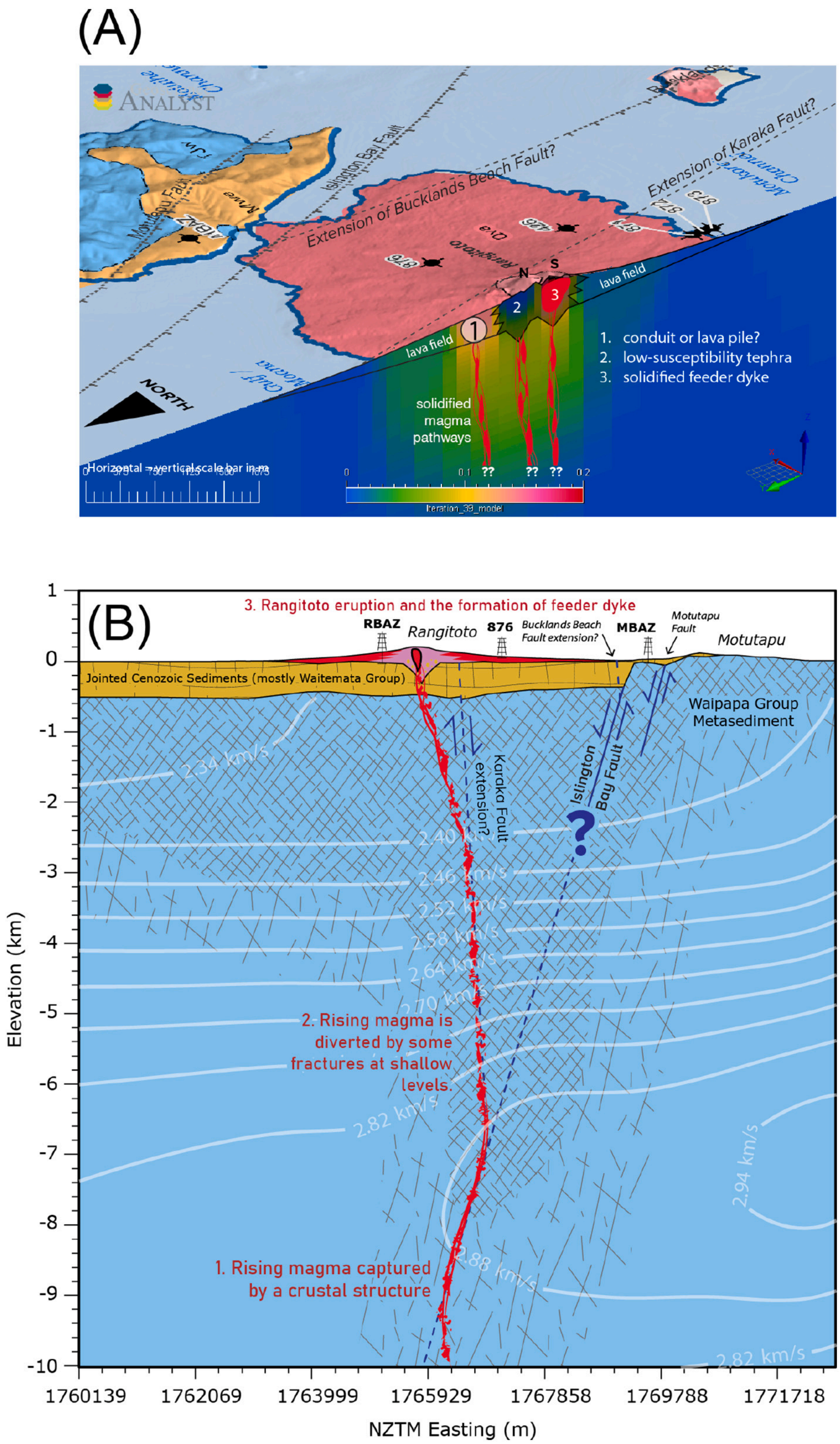

Fig. 11. A conceptual model of Rangitoto showing the geological and volcanological relevance of the models presented in this study. Figure (A) displays a schematic drawing of Rangitoto shallow subsurface volcanic features, interpreted from the north–south section of the 3D magnetic model, the compact end-member $[0, 1, 1, 1]$. Magnetic model cross-section is made using Geoscience ANALYST software. (B) West-east cross section of Rangitoto showing the magma captured by the a crustal structure at ~ 9 km deep, then diverted to another intersecting fracture at ~ 6 km depth and shallower, before it erupted as Rangitoto volcano. Magma diversion depth figures are indicative only. White contours show the crustal shear wave speed (in km/s) variation modelled for $>$ 500 m depths extracted from Ensing et al. (2022). Geological map and lithology colours in this figure follow from Fig. 1.

(Supplementary Material 4). This left the second interpretation, shown in Fig. 11A, that the model fails to resolve closely-separated individual magma pathways at greater depth, as the likelier explanation for the apparent bifurcation in the model. Resolution experiments with parallel pathways models, presented in the Supplementary Material 5, supports this argument.

4.2. *Crustal structures and its relationship to Rangitoto*

The Islington Bay Fault is mapped as a major NNW-SSE-trending basement fault with Rangitoto volcano on the downthrown block (Milligan, 1977; Kenny et al., 2012). Other large-scale faults, shear zones, and lithological heterogeneities may also be present within the basement, developed during the Permian to late Mesozoic accretionary tectonic regime (Eccles et al., 2005). Westward-dipping shear wave speed discontinuity at > 6 km depth under Rangitoto (Ensing et al., 2022) is associated with these NNW-SSE-trending structures.

In our 2.5D models, the Islington Bay Fault can be portrayed either as a steeply-dipping ($> 60^{\circ}$) reverse (Fig. 5B) or normal fault (Fig. 5C). We prefer a steeply westward-dipping normal fault model (Fig. 5C), for it is more consistent with the local geological context (Edbrooke, 2001; Kenny et al., 2012). In our preferred Islington Bay Fault model (Fig. 5C), we estimate that the fault has $\sim 300 \pm 50$ m of vertical displacement, similar to that (~ 270 m; EQC, 2012) from a set of NE–SW trending faults at the eastern end of Whangaparaoa Peninsula (Fig. 1B), 20 km north of Rangitoto. Extrapolation to depth of both the Islington Bay and Whangaparaoa faults could be associated with the same shear wave speed discontinuity in Ensing et al. (2022), signifying a potential linkage to deeper crustal structures. These deep crustal structures might still act as significant local weakness zones and, where reactivated, have generated several shallow (5–10 km deep) earthquakes since 2010 (GNS Science, 2022b).

Using our 2.5D gravity models, we can estimate that a planar, steeply westward-dipping Islington Bay would pass under the Rangitoto crater at > 6 km depth (Fig. 11), which coincides with the start of Ensing et al. (2022) velocity discontinuity. However, this planar extrapolation assumes geological continuity between the upper and lower parts of the crust, which may not be the case. A connection, or association between the Islington Bay Fault to older faults, shear zones, or lithological heterogeneities in the lower crusts inherited from the Mesozoic (Eccles et al., 2005) is also possible. Rising Rangitoto magma encountering those structures within the brittle crust ($< 15 - 20$ km depth; Sherburn et al., 2007) could either open the structures and utilise them to further propagate upward, or bypass them and keep opening its own pathway. The latter scenario is theoretically preferred when the structures become very stiff due to inactivity (Drymoni et al., 2021), which seismic catalogue (GNS Science, 2022b) indicates otherwise, or when the magma pressure fails to overcome normal stresses working on the structural plane (Martí et al., 2016). However, the latter scenario is also unlikely since the overpressure required by Rangitoto magma to pierce the crust will reach several hundred MPa (e.g. 500 MPa estimated for Pupuke Maar in the AVF; Brenna et al., 2018). Thus, the prospect of ascending Rangitoto magma opening up the deep crustal structure as a part of its pathway is still likely (Fig. 11B).

However, if deep crustal structures associated or connected with the Islington Bay Fault were a part of Rangitoto magma pathway, then why did the volcano erupt 3.5 km west of it (Fig. 1)? Magma flowing inside a structure can escape if the structure intersects another structure or the hanging wall becomes heavily fractured, especially at shallower depths (Gaffney et al., 2007, Supplementary Material 6). The hypothetical extension of Karaka Fault, which would pass directly beneath Rangitoto (Figs. 1, 9, 10), could locally intensify the fracture formation process in the already jointed Waipapa Group greywacke (Mayer, 1968; Edbrooke, 2001; Kermode, 1992). Joints of Waipapa Group greywacke are observable via Google Earth over Motutapu Island on the scale of tens of metres (Supplementary Material 6). This locally intensive fracture zone could provide an escape route for magma flowing inside the deep crustal structures associated or connected with the Islington Bay Fault (Fig. 11B). The role of fracture zone inside the Waipapa Group greywacke becomes more important if the hypothetical Karaka Fault extension does not exist, since it provides the only way for the magma to escape from deep crustal structure in the near-surface. In all cases, escape will be favourable at $\leqslant \sim 6$ km depths (Fig. 11B), where hanging wall fracture length required for magma escape is $\leqslant \sim 1$ m for most cases (Gaffney et al., 2007, Supplementary Material 6).

The dominance of structural control in directing the Rangitoto magma pathway in the shallow, brittle crust is reflected in the fault-parallel alignment of the northern and South Cone high susceptibility bodies (Fig. 10). Besides fractures, other local crustal weaknesses that might have also been exploited by ascending Rangitoto magma are shear zones and contacts between lithological heterogeneities in and around terrane boundaries indicated by the JMA (Fig. 1; Eccles et al., 2005; Hopkins et al., 2020).

5. Conclusion

Gravity and magnetic models reveal the shallow plumbing systems of Rangitoto and add new insight on the interaction between crustal structure and Rangitoto magma pathway. A presence of a shallow (< 300 m deep) basaltic body under the South Cone edifice is indicated by gravity and magnetic models. We interpret this body as a solidified feeder dyke. In the 3D magnetic models, another high susceptibility body exists north of this South Cone basaltic mass, which we interpret as a second possible conduit or lava pile.

Three-dimensional magnetic modelling of Rangitoto suggests the presence of two parallel, closely spaced magma pathways connected to the South Cone basaltic mass and northern high-susceptibility body. The fault-parallel alignment of the South Cone basaltic mass and northern high-susceptibility body suggests crustal structures have had a control on Rangitoto magma ascent pathways. We propose that as magma ascended through the upper crust it was captured by a structure before escaping through hanging wall fractures possibly provided by an intersection with the hypothetical northward extension of Karaka Fault or any other shallow (< 6 km depth) crustal fractures of sufficient length. This mechanism could explain why Rangitoto erupted ~ 3.5 km from the topographic expression of the Islington Bay Fault.

We recommend that further work be undertaken to map the locations and characteristics of basement faults concealed beneath the Miocene sediments in Auckland. In a more global context, the Rangitoto case indicates that (1) basement faults may influence the locations of future eruptions in the small-volume volcanic field, and (2) their eruptions may not happen along the fault trace, but offset from it. Hence, knowing the location and characteristics of concealed basement faults and intensity of fracturing are important in determining their role in future eruptions and establishing a possible buffer zone around them as high likelihood eruption locations.

CRediT authorship contribution statement

Alutsyah Luthfian: Conceptualization, Methodology, Formal-analysis, Investigation, Data-curation, Writing-original-draft, Writing-review-editing, Visualization, Project-administration. **Jennifer D. Eccles:** Conceptualization, Funding-acquisition, Supervision, Writing-review-editing, Resources. **Craig A. Miller:** Conceptualization, Supervision, Writing-review-editing, Resources.

Declaration of Competing Interest

The authors declare that they have no known competing financial interests or personal relationships that could have appeared to influence the work reported in this paper.

Data availability

Data used in this study are available as supplementary materials.

Acknowledgements

We would like to express our gratitude to Ngāi Tai ki Tāmaki iwi and the Department of Conservation for granting us permission to do our mahi with their taonga in their sacred conservation area. We feel obliged for the time and efforts spent by JD (Ngāi Tai ki Tāmaki taonga in Motutapu) and field assistants that helped complete Rangitoto gravity and GPS data acquisition: Bastian Steinke, J.R. Kuethe, Yuda Munarko, Edy Setyawan, Rizki Dian Rahayani, and Andi Batara Al Isra. This research is funded by the DEtermining VOlcanic Risk in Auckland

(DEVORA) research programme and The University of Auckland Postgraduate Research Student Support (PReSS). Craig Miller is supported by the Ministry of Business, Innovation and Employment (MBIE) Strategic Science Investment Fund, Hazards and Risk Management programme at GNS Science. We finally appreciate for the detailed reviews from Fabio Caratori-Tontini and Jim Kauahikaua that substantially improved the readability and scientific value of this manuscript.

Appendix A. Supplementary data

Supplementary data associated with this article can be found, in the online version, at https://doi.org/10.1016/j.jvolgeores.2023.107824. These data include Google maps of the most important areas described in this article.

References

Aboud, E., El-Masry, N., Qaddah, A., Alqahtani, F., Moufti, M.R.H., 2015. Magnetic and gravity data analysis of Rahat Volcanic Field, El-Madinah city, Saudi Arabia. NRIAG J. Astron. Geophys. 4, 154–162. https://doi.org/10.1016/j.nrjag.2015.06.006.

Affleck, D.K., Cassidy, J., Locke, C.A., 2001. Te Pouhawaiki Volcano and pre-volcanic topography in central Auckland: Volcanological and hydrogeological implications. N.Z. J. Geol. Geophys. 44, 313–321. https://doi.org/10.1080/00288306.2001.9514940.

Alken, P., Thébault, E., Beggan, C.D., Amit, H., Aubert, J., Baerenzung, J., Bondar, T.N., Brown, W.J., Califf, S., Chambodut, A., Chulliat, A., Cox, G.A., Finlay, C.C., Fournier, A., Gillet, N., Grayver, A., Hammer, M.D., Holschneider, M., Huder, L., Hulot, G., Jager, T., Kloss, C., Korte, M., Kuang, W., Kuvshinov, A., Langlais, B., Léger, J.M., Lesur, V., Livermore, P.W., Lowes, F.J., Macmillan, S., Magnes, W., Mandea, M., Marsal, S., Matzka, J., Metman, M.C., Minami, T., Morschhauser, A., Mound, J.E., Nair, M., Nakano, S., Olsen, N., Pavón-Carrasco, F.J., Petrov, V.G., Ropp, G., Rother, M., Sabaka, T.J., Sanchez, S., Saturnino, D., Schnepf, N.R., Shen, X., Stolle, C., Tangborn, A., Tøffner-Clausen, L., Toh, H., Torta, J.M., Varner, J., Vervelidou, F., Vigneron, P., Wardinski, I., Wicht, J., Woods, A., Yang, Y., Zeren, Z., Zhou, B., 2021. International Geomagnetic Reference Field: the thirteenth generation. Earth Planets Space 73. https://doi.org/10.1186/s40623-020.

Barde-Cabusson, S., Gottsmann, J., Martí, J., Bolós, X., Camacho, A.G., Geyer, A., Planagumà, L., Ronchin, E., Sánchez, A., 2013. Structural control of monogenetic volcanism in the Garrotxa volcanic field (Northeastern Spain) from gravity and self-potential measurements. Bull. Volcanol. 76 https://doi.org/10.1007/s00445-013-0788-0.

Bebbington, M.S., 2015. Spatio-volumetric hazard estimation in the Auckland volcanic field. Bull. Volcanol. 77 https://doi.org/10.1007/s00445-015-0921-3.

Blaikie, T.N., Ailleres, L., Betts, P.G., Cas, R.A.F., 2014. Interpreting subsurface volcanic structures using geologically constrained 3-D gravity inversions: Examples of maar-diatremes, Newer Volcanics Province, southeastern Australia. J. Geophys. Res.: Solid Earth 119, 3857–3878. https://doi.org/10.1002/2013jb010751.

Blakely, R.J., 1995. Potential Theory in Gravity and Magnetic Applications, 1st ed. Cambridge University Press, Cambridge, United Kingdom.

Boivin, P., Thouret, J.C., 2013. The Volcanic Chaîne des Puys: A Unique Collection of Simple and Compound Monogenetic Edifices. In: World Geomorphological Landscapes. Springer, Netherlands, pp. 81–91. https://doi.org/10.1007/978-94-007-7022-5_9.

Brenna, M., Cronin, S.J., Németh, K., Smith, I.E.M., Sohn, Y.K., 2011. The influence of magma plumbing complexity on monogenetic eruptions, Jeju Island, Korea. Terra Nova 23, 70–75. https://doi.org/10.1111/j.1365-3121.2010.00985.x.

Brenna, M., Cronin, S.J., Smith, I.E.M., Tollan, P.M.E., Scott, J.M., Prior, D.J., Bambery, K., Ukstins, I.A., 2018. Olivine xenocryst diffusion reveals rapid monogenetic basaltic magma ascent following complex storage at Pupuke Maar, Auckland Volcanic Field, New Zealand. Earth Planet. Sci. Lett. 499, 13–22. https://doi.org/10.1016/j.epsl.2018.07.015.

Carracedo-Sánchez, M., Sarrionandia, F., Ábalos, B., Errandonea-Martin, J., Ibarguchi, J. I.G., 2017. Intra-cone plumbing system and eruptive dynamics of small-volume basaltic volcanoes: A case study in the Calatrava Volcanic Field. J. Volcanol. Geoth. Res. 348, 82–95. https://doi.org/10.1016/j.jvolgeores.2017.10.014.

Cassidy, J., France, S.J., Locke, C.A., 2007. Gravity and magnetic investigation of maar volcanoes, Auckland volcanic field, New Zealand. J. Volcanol. Geoth. Res. 159, 153–163. https://doi.org/10.1016/j.jvolgeores.2006.06.007.

Cassidy, J., Locke, C.A., 2010. The Auckland volcanic field, New Zealand: Geophysical evidence for structural and spatio-temporal relationships. J. Volcanol. Geoth. Res. 195, 127–137. https://doi.org/10.1016/j.jvolgeores.2010.06.016.

Cocchi, L., Passaro, S., Tontini, F.C., Ventura, G., 2017. Volcanism in slab tear faults is larger than in island-arcs and back-arcs. Nat. Commun. 8 https://doi.org/10.1038/s41467-017-01626-w.

Cockett, R., Kang, S., Heagy, L.J., Pidlisecky, A., Oldenburg, D.W., 2015. SimPEG: An open source framework for simulation and gradient based parameter estimation in geophysical applications. Comput. Geosci. 85, 142–154. https://doi.org/10.1016/j.cageo.2015.09.015.

Corvec, N.L., Spörli, K.B., Rowland, J., Lindsay, J., 2013. Spatial distribution and alignments of volcanic centers: Clues to the formation of monogenetic volcanic fields. Earth Sci. Rev. 124, 96–114. https://doi.org/10.1016/j.earscirev.2013.05.005.

Delaney, P.T., Pollard, D.D., Ziony, J.I., McKee, E.H., 1986. Field relations between dikes and joints: Emplacement processes and paleostress analysis. J. Geophys. Res. 91, 4920. https://doi.org/10.1029/jb091ib05p04920.

Drymoni, K., Browning, J., Gudmundsson, A., 2021. Volcanotectonic interactions between inclined sheets, dykes, and faults at the Santorini Volcano, Greece. J. Volcanol. Geoth. Res. 416, 107294 https://doi.org/10.1016/j.jvolgeores.2021.107294.

Duncan, R.A., Kent, A.J.R., Thornber, C.R., Schlieder, T.D., Al-Amri, A.M., 2016. Timing and composition of continental volcanism at Harrat Hutaymah, western Saudi Arabia. J. Volcanol. Geoth. Res. 313, 1–14. https://doi.org/10.1016/j.jvolgeores.2016.01.010.

Eccles, J.D., 2003. Structural and tectonic implications of the junction magnetic anomaly in the Auckland Region. Master's thesis. The University of Auckland, Auckland, New Zealand.

Eccles, J.D., Cassidy, J., Locke, C.A., Spörli, K.B., 2005. Aeromagnetic imaging of the Dun Mountain Ophiolite Belt in northern New Zealand: insight into the fine structure of a major SW Pacific terrane suture. J. Geol. Soc. 162, 723–735. https://doi.org/10.1144/0016-764904-060.

Edbrooke, S.W., 2001. Geology of the Auckland Area. In: Institute of Geological and Nuclear Sciences 1:250 000 Geological Map, vol. 3. Institute of Geological and Nuclear Sciences Limited, Lower Hutt, New Zealand.

Elshaafi, A., Gudmundsson, A., 2016. Volcano-tectonics of the Al Haruj Volcanic Province, Central Libya. J. Volcanol. Geoth. Res. 325, 189–202. https://doi.org/10.1016/j.jvolgeores.2016.06.025.

Ensing, J.X., van Wijk, K., Spörli, K.B., 2022. A 3D crustal shear speed model of the Auckland volcanic field, New Zealand, from multi-component ambient noise tomography. Tectonophysics 845, 229627. https://doi.org/10.1016/j.tecto.2022.229627.

EQC, 2012. New Zealand Geotechnical Database. URL:https://www.nzgd.org.nz/.

Espindola, J.M., Lopez-Loera, H., Mena, M., Zamora-Camacho, A., 2016. Internal architecture of the Tuxtla volcanic field, Veracruz, Mexico, inferred from gravity and magnetic data. J. Volcanol. Geoth. Res. 324, 15–27. https://doi.org/10.1016/j.jvolgeores.2016.05.006.

Foote, A., Németh, K., Handley, H., 2022. The interplay between environmental and magmatic conditions in eruption style transitions within a fissure-aligned monogenetic volcanic system of Auckland, New Zealand. J. Volcanol. Geoth. Res. 431, 107652 https://doi.org/10.1016/j.jvolgeores.2022.107652.

Fournier, D., Heagy, L.J., Oldenburg, D.W., 2020. Sparse magnetic vector inversion in spherical coordinates. Geophysics 85, J33–J49. https://doi.org/10.1190/geo2019-0244.1.

Fournier, D., Oldenburg, D.W., 2019. Inversion using spatially variable mixed ℓp norms. Geophys. J. Int. 218, 268–282. https://doi.org/10.1093/gji/ggz156.

France, L., Demacon, M., Gurenko, A.A., Briot, D., 2016. Oxygen isotopes reveal crustal contamination and a large, still partially molten magma chamber in Chaîne des Puys (French Massif Central). Lithos 260, 328–338. https://doi.org/10.1016/j.lithos.2016.05.013.

Gaffney, E.S., Damjanac, B., Valentine, G.A., 2007. Localization of volcanic activity: 2. effects of pre-existing structure. Earth Planet. Sci. Lett. 263, 323–338. https://doi.org/10.1016/j.epsl.2007.09.002.

GNS Science, 2012. NZ land gravity database. URL:https://data.gns.cri.nz/metadata/srv/eng/catalog.search#/metadata/D4AA56B8-8DBD-4EC6-A292-7F90D55E751D, doi: 10.21420/DRDW-VC72.

GNS Science, 2020. NZL GNS 1:250K Geology. URL:https://data.gns.cri.nz/metadata/srv/eng/catalog.search#/metadata/5F6780CB-4135-4204-A2C8-50DD74B0466F, doi: 10.21420/JEAP-4J81.

GNS Science, 2022a. GeoNet Aotearoa New Zealand Continuous GNSS Network - RINEX Files. URL:https://data.gns.cri.nz/metadata/srv/eng/catalog.search#/metadata/86930f0a-f96c-436d-9315-d3e291a171ed, doi: 10.21420/RXKE-AZ44. Accessed: 2022-12-14.

GNS Science, 2022b. GeoNet Aotearoa New Zealand Earthquake Catalogue. URL: https://data.gns.cri.nz/metadata/srv/eng/catalog.search#/metadata/5105fdeb-f314-4d6e-8e09-bf5308278e03, doi: 10.21420/0S8P-TZ38. Accessed: 2022-12-15.

Gómez-Vasconcelos, M.G., Macías, J.L., Avellán, D.R., Sosa-Ceballos, G., Garduño-Monroy, V.H., Cisneros-Máximo, G., Layer, P.W., Benowitz, J., López-Loera, H., López, F.M., Perton, M., 2020. The control of preexisting faults on the distribution, morphology, and volume of monogenetic volcanism in the Michoacán-Guanajuato Volcanic Field. GSA Bull. 132, 2455–2474. https://doi.org/10.1130/b35397.1.

Guffanti, M., Clynne, M.A., Smith, J.G., Muffler, L.J.P., Bullen, T.D., 1990. Late Cenozoic volcanism, subduction, and extension in the Lassen Region of California, southern Cascade Range. J. Geophys. Res. 95, 19453. https://doi.org/10.1029/jb095ib12p19453.

Hall, A., 2013. Ko Rangitoto, Ko Waitemata: Cultural landmarks for the integration of a Maori indigenous psychotherapy in Aotearoa. Ata J. Psychother. Aotearoa N.Z. 17, 139–157. https://doi.org/10.9791/ajpanz.2013.14.

Hastings, M.S., Connor, C.B., Wetmore, P., Malservisi, R., Connor, L.J., Rodgers, M., Femina, P.C.L., 2021. Large-Volume and Shallow Magma Intrusions in the Blackfoot Reservoir Volcanic Field (Idaho, USA). J. Geophys. Res.: Solid Earth 126. https://doi.org/10.1029/2021jb022507.

Hayward, B.W., 2017. Eruption sequence of Rangitoto Volcano, Auckland. Geosci. Soc. N.Z. Newslett. 23, 4–10. URL:https://ndhadeliver.natlib.govt.nz/delivery/DeliveryManagerServlet?dps_pid=IE36424062.

Hayward, B.W., 2019. Volcanoes of Auckland: A Field Guide. Auckland University Press. URL:https://auckland.primo.exlibrisgroup.com/permalink/64UAUCK_INST/13vfdcn/alma99265184314002091. Aerial photography by Alastair Jamieson.

Hayward, B.W., Brook, F.J., 1984. Lithostratigraphy of the basal Waitemata Group, Kawau Subgroup (new), Auckland, New Zealand. N.Z. J. Geol. Geophys. 27, 101–123. https://doi.org/10.1080/00288306.1984.10422521.
Hayward, B.W., Hopkins, J.L., Morley, M., Kenny, J.A., 2022. Microfossil evidence for a possible maar crater and tuff ring beneath Rangitoto Volcano, Auckland, New Zealand. N.Z. J. Geol. Geophys. 1–17 https://doi.org/10.1080/00288306.2022.2120505.
Hinze, W.J., Aiken, C., Brozena, J., Coakley, B., Dater, D., Flanagan, G., Forsberg, R., Hildenbrand, T., Keller, G.R., Kellogg, J., Kucks, R., Li, X., Mainville, A., Morin, R., Pilkington, M., Plouff, D., Ravat, D., Roman, D., Urrutia-Fucugauchi, J., Véronneau, M., Webring, M., Winester, D., 2005. New standards for reducing gravity data: The North American gravity database. Geophysics 70, J25–J32. https://doi.org/10.1190/1.1988183.
Hinze, W.J., von Frese, R.R.B., Saad, A.H., 2013. Gravity and Magnetic Exploration: Principles, Practices, and Applications, 1st ed. Cambridge University Press, Cambridge, United Kingdom.
Holt, S.J., Holford, S.P., Foden, J., 2013. New insights into the magmatic plumbing system of the South Australian Quaternary Basalt province from 3D seismic and geochemical data. Aust. J. Earth Sci. 60, 797–817. https://doi.org/10.1080/08120099.2013.865143.
Hopkins, J.L., Smid, E.R., Eccles, J.D., Hayes, J.L., Hayward, B.W., McGee, L.E., van Wijk, K., Wilson, T.M., Cronin, S.J., Leonard, G.S., Lindsay, J.M., Németh, K., Smith, I.E.M., 2020. Auckland Volcanic Field magmatism, volcanism, and hazard: a review. N.Z. J. Geol. Geophys. 64, 1–22. https://doi.org/10.1080/00288306.2020.1736102.
Hopkins, J.L., Wilson, C.J.N., Millet, M.A., Leonard, G.S., Timm, C., McGee, L.E., Smith, I.E.M., Smith, E.G.C., 2017. Multi-criteria correlation of tephra deposits to source centres applied in the Auckland Volcanic Field, New Zealand. Bull. Volcanol. 79 https://doi.org/10.1007/s00445-017-1131-y.
Houghton, B.F., Schmincke, H.U., 1989. Rothenberg scoria cone, East Eifel: a complex Strombolian and phreatomagmatic volcano. Bull. Volcanol. 52, 28–48. https://doi.org/10.1007/bf00641385.
van den Hove, J., Grose, L., Betts, P.G., Ailleres, L., Otterloo, J.V., Cas, R.A.F., 2017. Spatial analysis of an intra-plate basaltic volcanic field in a compressional tectonic setting: South-eastern Australia. J. Volcanol. Geoth. Res. 335, 35–53. https://doi.org/10.1016/j.jvolgeores.2017.02.001.
Huang, Y., Hawkesworth, C., van Calsteren, P., Smith, I., Black, P., 1997. Melt generation models for the Auckland volcanic field, New Zealand: constraints from UTh isotopes. Earth Planet. Sci. Lett. 149, 67–84. https://doi.org/10.1016/S0012-821X(97)00064-2.
Hunt, T.M., Syms, M.C., 1977. Sheet 3, auckland. Printed map. URL:https://natlib-primo.hosted.exlibrisgroup.com/permalink/f/1s57t7d/NLNZ_ALMA21231825360002836.
Johannes, W.J., Smilde, P.L., 2009. Gravity Interpretation. Springer Berlin Heidelberg. https://doi.org/10.1007/978-3-540-85329-9.
Kane, M.F., 1962. A Comprehensive System of Terrain Corrections Using A Digital Computer. Geophysics 27, 455–462. https://doi.org/10.1190/1.1439044.
Kenny, J., 2013a. An Exercise in Untangling the Complex Geology of Northern Auckland Using Simple LiDAR. Geocene: Auckland GeoClub Mag. 10, 2–9. URL:https://ndhadeliver.natlib.govt.nz/delivery/DeliveryManagerServlet?dps_pid=IE55696138.
Kenny, J., 2013b. Northward Tilting of the Waitemata Group Erosion Surface in the Auckland Region. Geocene: Auckland GeoClub Mag. 9, 2–6. URL:https://ndhadeliver.natlib.govt.nz/delivery/DeliveryManagerServlet?dps_pid=IE55696183.
Kenny, J., Lindsay, J., Howe, T., 2012. Post-Miocene faults in Auckland: insights from borehole and topographic analysis. N.Z. J. Geol. Geophys. 55, 323–343. https://doi.org/10.1080/00288306.2012.706618.
Kenny, J.A., Lindsay, J.M., Howe, T.M., 2011. Large-Scale Faulting in the Auckland Region. Technical Report. Institute of Earth Science and Engineering, Auckland, New Zealand.
Kereszturi, G., Németh, K., 2016. Sedimentology, eruptive mechanism and facies architecture of basaltic scoria cones from the Auckland Volcanic Field (New Zealand). J. Volcanol. Geoth. Res. 324, 41–56. https://doi.org/10.1016/j.jvolgeores.2016.05.012.
Kereszturi, G., Németh, K., Cronin, S.J., Agustín-Flores, J., Smith, I.E.M., Lindsay, J., 2013. A model for calculating eruptive volumes for monogenetic volcanoes — Implication for the Quaternary Auckland Volcanic Field, New Zealand. J. Volcanol. Geoth. Res. 266, 16–33. https://doi.org/10.1016/j.jvolgeores.2013.09.003.
Kermode, L.E., 1992. Geology of the Auckland Urban Area. Institute of Geological and Nuclear Sciences Geological Map 2. Institute of Geological and Nuclear Sciences Limited, Lower Hutt, New Zealand, 1 sheet + 63p.
Korte, M., Constable, C., 2011. Improving geomagnetic field reconstructions for 0–3ka. Phys. Earth Planet. Inter. 188, 247–259. https://doi.org/10.1016/j.pepi.2011.06.017.
Leonard, G.S., Calvert, A.T., Hopkins, J.L., Wilson, C.J.N., Smid, E.R., Lindsay, J.M., Champion, D.E., 2017. High-precision 40Ar/39Ar dating of Quaternary basalts from Auckland Volcanic Field, New Zealand, with implications for eruption rates and paleomagnetic correlations. J. Volcanol. Geoth. Res. 343, 60–74. https://doi.org/10.1016/j.jvolgeores.2017.05.033.
Linnell, T., Shane, P., Smith, I., Augustinus, P., Cronin, S., Lindsay, J., Maas, R., 2016. Long-lived shield volcanism within a monogenetic basaltic field: The conundrum of Rangitoto volcano, New Zealand. Geol. Soc. Am. Bull. 128, 1160–1172. https://doi.org/10.1130/b31392.1.
LINZ, 2016a. Auckland LiDAR 1m DEM (2013). URL:https://data.linz.govt.nz/layer/53405-auckland-lidar-1m-dem-2013/metadata/?type=dc. Accessed: 2022-12-14.
LINZ, 2016b. NZ 8m Digital Elevation Model (2012). URL:https://data.linz.govt.nz/layer/51768-nz-8m-digital-elevation-model-2012/metadata/?type=dc. Accessed: 2022-12-14.
Mackay, K.A., Mackay, E.J., Neil, H.L., Mitchell, J.S., Bardsley, S.A., 2012. Hauraki Gulf. Map and offline digital data. URL:https://niwa.co.nz/our-science/oceans/bathymetry/further-information#hauraki-bathymetry.
Martí, J., López, C., Bartolini, S., Becerril, L., Geyer, A., 2016. Stress controls of monogenetic volcanism: A review. Front. Earth Sci. 4 https://doi.org/10.3389/feart.2016.00106.
Mayer, W., 1968. The Stratigraphy and Structure of the Waipapa Group on the Islands of Motutapu, Rakino, and the Noisies Group near Auckland, New Zealand. Trans. R. Soc. N.Z.: Geol. 5, 215–233. URL:https://paperspast.natlib.govt.nz/periodicals/transactions-of-the-royal-society-of-new-zealand-geology/1968/01/30/1.
Mayer, W., 1969. Petrology of the Waipapa Group, near Auckland, New Zealand. N.Z. J. Geol. Geophys. 12, 412–435. https://doi.org/10.1080/00288306.1969.10420291.
Mazzarini, F., 2003. Spatial distribution of cones and satellite-detected lineaments in the Pali Aike Volcanic Field (southernmost Patagonia): insights into the tectonic setting of a Neogene rift system. J. Volcanol. Geoth. Res. 125, 291–305. https://doi.org/10.1016/s0377-0273(03)00120-3.
McCubbine, J., Tontini, F.C., Stagpoole, V., Smith, E., O'Brien, G., 2018. Gsolve, a Python computer program with a graphical user interface to transform relative gravity survey measurements to absolute gravity values and gravity anomalies. SoftwareX 7, 129–137. https://doi.org/10.1016/j.softx.2018.04.003.
Miller, C.A., Schaefer, L.N., Kereszturi, G., Fournier, D., 2020. Three-Dimensional Mapping of Mt. Ruapehu Volcano, New Zealand, From Aeromagnetic Data Inversion and Hyperspectral Imaging. J. Geophys. Res.: Solid Earth 125. https://doi.org/10.1029/2019jb018247.
Miller, C.A., Williams-Jones, G., Fournier, D., Witter, J., 2017. 3d gravity inversion and thermodynamic modelling reveal properties of shallow silicic magma reservoir beneath laguna del maule, chile. Earth Planet. Sci. Lett. 459, 14–27. https://doi.org/10.1016/j.epsl.2016.11.007.
Milligan, J.A., 1977. A geophysical study of Rangitoto volcano. Master's thesis. The University of Auckland, Auckland, New Zealand.
Nagy, D., 1966. The gravitational attraction of a right rectangular prism. Geophysics 31, 362–371. https://doi.org/10.1190/1.1439779.
Needham, A.J., Lindsay, J.M., Smith, I.E.M., Augustinus, P., Shane, P.A., 2011. Sequential eruption of alkaline and sub-alkaline magmas from a small monogenetic volcano in the Auckland Volcanic Field, New Zealand. J. Volcanol. Geoth. Res. 201, 126–142. https://doi.org/10.1016/j.jvolgeores.2010.07.017.
Nettleton, L.L., 1939. Determination of density for reduction of gravimeter observations. Geophysics 4, 176–183. https://doi.org/10.1190/1.0403176.
Nunns, A.G., Hochstein, M.P., 2019. Geophysical constraints on the structure and formation of Onepoto, Orakei, Pupuke and Tank Farm maar volcanoes, Auckland Volcanic Field. N.Z. J. Geol. Geophys. 62, 341–356. https://doi.org/10.1080/00288306.2019.1581239.
Paoletti, V., Maio, R.D., Cella, F., Florio, G., Motschka, K., Roberti, N., Secomandi, M., Supper, R., Fedi, M., Rapolla, A., 2009. The Ischia volcanic island (Southern Italy): Inferences from potential field data interpretation. J. Volcanol. Geoth. Res. 179, 69–86. https://doi.org/10.1016/j.jvolgeores.2008.10.008.
Petronis, M.S., Delcamp, A., van Wyk de Vries, B., 2013. Magma emplacement into the lemptégy scoria cone (chaîne des puys, france) explored with structural, anisotropy of magnetic susceptibility, and paleomagnetic data. Bull. Volcanol. 75 https://doi.org/10.1007/s00445-013-0753-y.
Rivalta, E., Taisne, B., Bunger, A.P., Katz, R.F., 2015. A review of mechanical models of dike propagation: Schools of thought, results and future directions. Tectonophysics 638, 1–42. https://doi.org/10.1016/j.tecto.2014.10.003.
Robertson, D.J., 1983. Paleomagnetism and geochronology of volcanics in the northern North Island, New Zealand. Ph.D. thesis. The University of Auckland, Auckland, New Zealand.
Robertson, D.J., 1986. A paleomagnetic study of Rangitoto Island, Auckland, New Zealand. N.Z. J. Geol. Geophys. 29, 405–411. https://doi.org/10.1080/00288306.1986.10422162.
Rosas-Carbajal, M., Jourde, K., Marteau, J., Deroussi, S., Komorowski, J.C., Gibert, D., 2017. Three-dimensional density structure of La Soufrière de Guadeloupe lava dome from simultaneous muon radiographies and gravity data. Geophys. Res. Lett. 44, 6743–6751. https://doi.org/10.1002/2017gl074285.
Ross, P.S., Delpit, S., Haller, M.J., Németh, K., Corbella, H., 2011. Influence of the substrate on maar-diatreme volcanoes — An example of a mixed setting from the Pali Aike volcanic field, Argentina. J. Volcanol. Geoth. Res. 201, 253–271. https://doi.org/10.1016/j.jvolgeores.2010.07.018.
Seequent Limited, 2020. Computational Basis for GM-SYS. URL:https://my.seequent.com/support/.
Sherburn, S., Scott, B.J., Olsen, J., Miller, C., 2007. Monitoring seismic precursors to an eruption from the Auckland Volcanic Field, New Zealand. N.Z. J. Geol. Geophys. 50, 1–11. https://doi.org/10.1080/00288300709509814.
Shibuya, H., Cassidy, J., Smith, I.E.M., Itaya, T., 1992. A geomagnetic excursion in the Brunhes epoch recorded in New Zealand basalts. Earth Planet. Sci. Lett. 111, 41–48. https://doi.org/10.1016/0012-821x(92)90167-t.
Skeels, D.C., 1947. Ambiguity in gravity interpretation. Geophysics 12, 43–56. https://doi.org/10.1190/1.1437295.
Smith, I.E.M., Németh, K., 2017. Source to surface model of monogenetic volcanism: a critical review. Geol. Soc. Lond. Spec. Publ. 446, 1–28. https://doi.org/10.1144/sp446.14.
Spörli, B.K., 1989. Tectonic framework of Northland, New Zealand. In: Spörli, B.K., Kear, D. (Eds.), Geology of Northland: accretion, allochthons and arcs at the edge of the New Zealand micro-continent, vol. 26. The Royal Society of New Zealand, pp. 3–14.

Spörli, K., Black, P., Lindsay, J., 2015. Excavation of buried Dun Mountain-Maitai terrane ophiolite by volcanoes of the Auckland Volcanic field, New Zealand. N.Z. J. Geol. Geophys. 58, 229–243. https://doi.org/10.1080/00288306.2015.1035285.

Spörli, K.B., Rowland, J.V., 2007. Superposed deformation in turbidites and syn-sedimentary slides of the tectonically active Miocene Waitemata Basin, northern New Zealand. Basin Res. 19, 199–216. https://doi.org/10.1111/j.1365-2117.2007.00320.x.

Stagpoole, V., Tontini, F.C., Fukuda, Y., Woodward, D., 2021. New Zealand gravity reference stations 2020: history and development of the gravity network. N.Z. J. Geol. Geophys. 65, 362–373. https://doi.org/10.1080/00288306.2021.1886120.

Strong, D., Turnbull, R., Haubrock, S., Mortimer, N., 2016. Petlab: New Zealand's national rock catalogue and geoanalytical database. N.Z. J. Geol. Geophys. 59, 475–481. https://doi.org/10.1080/00288306.2016.1157086.

Talwani, M., Heirtzler, J.R., 1964. Computation of magnetic anomalies caused by two dimensional bodies of arbitrary shape. In: Parks, G.A. (Ed.), Computers in the Mineral Industries, Part 1, Geological Sciences, vol. 9. Stanford University Publishing, pp. 464–480.

Talwani, M., Worzel, J.L., Landisman, M., 1959. Rapid gravity computations for two-dimensional bodies with application to the mendocino submarine fracture zone. J. Geophys. Res. 64, 49–59. https://doi.org/10.1029/jz064i001p00049.

Trevino, S.F., Miller, C.A., Tikoff, B., Fournier, D., Singer, B.S., 2021. Multiple, coeval silicic magma storage domains beneath the laguna del maule volcanic field inferred from gravity investigations. J. Geophys. Res.: Solid Earth 126. https://doi.org/10.1029/2020jb020850.

UBC-GIF, 2018a. Data Misfit and Uncertainties. URL:https://giftoolscookbook.readthedocs.io/en/latest/content/fundamentals/Uncertainties.html.

UBC-GIF, 2018b. Sparse and Blocky Norms. URL:https://giftoolscookbook.readthedocs.io/en/latest/content/fundamentals/Norms.html.

UBC-GIF, 2018c. The Weighting Matrices W. URL:https://giftoolscookbook.readthedocs.io/en/latest/content/fundamentals/WeightingMatrix.html.

Williams, H.A., Cassidy, J., Locke, C.A., Spörli, K.B., 2006. Delineation of a large ultramafic massif embedded within a major SW pacific suture using gravity methods. Tectonophysics 424, 119–133. https://doi.org/10.1016/j.tecto.2006.07.009.

Yu, H., Xu, J., Zhao, B., Wei, F., 2020. Magmatic systems beneath Ashikule volcanic cluster (Western Kunlun, China): insights from compositional and textural features of lavas. Arab. J. Geosci. 13 https://doi.org/10.1007/s12517-020-05506-4.